J. Fluid Mech. (2011), *vol.* 682, *pp.* 304–331. © Cambridge University Press 2011
doi:10.1017/jfm.2011.226

Nonlinear transient growth in a vortex column

FAZLE HUSSAIN†, DHOORJATY S. PRADEEP AND ERIC STOUT

Department of Mechanical Engineering, University of Houston, Houston, TX 77204-4006, USA

(Received 15 December 2010; revised 16 March 2011; accepted 11 May 2011; first published online 19 July 2011)

Growth of optimal transient perturbations to an Oseen vortex column into the nonlinear regime is studied via direct numerical simulation (DNS) for Reynolds number, Re ($\equiv$ circulation/viscosity), up to 10 000. An optimal bending-wave transient mode is obtained from linear analysis and used as the initial condition. (DNS of a vortex column embedded in finer-scale turbulence reveals that optimal modes are preferentially excited during vortex–turbulence interaction.) Tilting of the optimal mode's radial vorticity perturbation into the azimuthal direction and its concomitant stretching by the column's strain field produces positive Reynolds stress, hence kinetic energy growth. Modes experiencing the largest growth are those with initial vorticity localized at a 'critical radius' outside the core, such that this perturbation vorticity resonantly induces core waves. Resonant forcing leads to growth of perturbation energy concentrated within the core. Moderate-amplitude ($\sim$5 %) perturbations cause significant distortion of the core and generate secondary filament-like spiral structures ('threads') outside the core. As the mode evolves into the nonlinear regime, radially outward self-advection of thread dipoles accelerates growth arrest by removing the perturbation from the critical radius and disrupting resonant forcing. With increasing Re, the evolving vorticity patterns become more chaotic, more turbulent-like (finer scaled, contorted vorticity), and persist longer. This suggests that at typical Re ($\sim 10^6$), nonlinear transient growth may indeed be able to break up, hence induce rapid decay of, column vortices – highly relevant for addressing the aircraft wake hazard crisis and the looming air traffic capacity crisis. In addition, we discover a regenerative transient growth scenario in which threads induce secondary perturbations closer to the vortex column. A parent–offspring regenerative mechanism is postulated and verified by DNS. There is a clear trend towards stronger regenerative growth with increasing Re. These results, showing an important role of transient growth in turbulent vortex decay, are highly relevant to the prediction and control of vortex-dominated flows.

Key words: transition to turbulence, vortex dynamics, vortex instability

1. Introduction

In many engineering flows it is important to accurately predict the evolution of large-scale organized vortices (coherent structures, CS), since these naturally occurring structures dominate phenomena of practical interest, such as mixing, drag, heat transfer and aeroacoustic noise. An important and, to date, inadequately understood aspect of CS dynamics is the nature of the interaction between the large-scale vortices and finer-scale turbulence.

† Email address for correspondence: fhussain@uh.edu

https://doi.org/10.1017/jfm.2011.226 Published online by Cambridge University Press

A prominent example is vortex–turbulence interaction in the aircraft wake. The intense tip vortices shed by large aircraft pose considerable hazard to trailing aircraft. Predicting the decay rate of these vortices is necessary to determine safe inter-aircraft spacings – the pacing factor controlling air traffic capacity. This crisis – not only during takeoffs and landings, but also during cruise – can most probably be mitigated by developing methods for forcing faster vortex decay. The mechanisms of trailing vortex decay are complex, involving cooperative instabilities, such as the Crow and elliptical instabilities, between conjugate tip vortices; the ground effect; effect of mean wind shear; interaction with turbulence, which may be vortex-generated or atmospheric; and transient growth of perturbations, either within a single vortex – see Antkowiak & Brancher (2004) and Pradeep & Hussain (2006, hereafter PH06) – or due to the interaction between different vortices in dipole pairs (Crouch 1997; Fabre, Jacquin & Loof 2002). State-of-the-art models used in practice remain largely empirical (Spalart 1998).

Focusing on the effect of turbulence on a single large-scale vortex (without axial flow), modeling efforts (Zeman 1995; Marshall & Beninati 2000; Wallin & Girimaji 2000) have attempted to predict basic quantities such as mean flow profiles, turbulence intensities and Reynolds stress distributions. There are considerable disagreements across models. For instance, Zeman (1995) found monotonic decay of turbulence around the vortex, with complete suppression of turbulence intensities and Reynolds stresses after approximately 100 turnover times. The vortex decays, consequently, at a viscous rate (as a laminar flow). Other studies (e.g. Wallin & Girimaji 2000) found that whether the initial turbulence grows or decays depends on its initial intensity: weak turbulence is amplified and intense turbulence damped. They predicted that the turbulence attains an equilibrium state that is roughly independent of the initial condition. The decay rates obtained in this study are larger than the viscous rate of decay.

The recent experimental study of Bailey & Tavoularis (2008) found that 'meandering' of a turbulent trailing vortex has a single dominant wavelength regardless of free-stream turbulence intensity. This seems to indicate that the vortex response to turbulence involves preferential excitation of specific waves. We may speculate that these are transient growth modes. While the Bailey–Tavoularis vortex features axial flow, there is evidence that vortices with and without axial flow share the underlying mechanisms governing vortex response. For example, a normal-mode-stable Batchelor vortex, i.e. a vortex with weak axial velocity compared to swirl velocity, generates transiently growing bending waves through a resonant-forcing mechanism (Heaton & Peake 2007), very similar to that seen in an Oseen vortex, discussed in PH06 and also later in this paper.

Results obtained by Pradeep & Hussain (2010, hereafter PH10) from direct numerical simulations (DNS) of a vortex column embedded in turbulence are not in complete agreement with turbulence models (discussed above). While DNS show that a turbulent vortex does decay at a nearly viscous rate and does not attain an equilibrium structure, the decay of turbulence need not be monotonic and the vortex can amplify perturbations if they are initially weak. This enigmatic, viscous decay of a turbulent vortex, in marked contrast to other turbulent free-shear flows such as plane jets and wakes, requires explanation. The likely reason for such slow decay is that fluctuations within the core evolve as inertial vortex waves, which can be intense without generating appreciable Reynolds stress (PH10). Significant Reynolds stress is required for faster-than-viscous decay (Zeman 1995). DNS of this stable flow show that fluctuation levels in the core exceed ambient turbulence intensity, indicating that an 'instability' is at play.

https://doi.org/10.1017/jfm.2011.226 Published online by Cambridge University Press

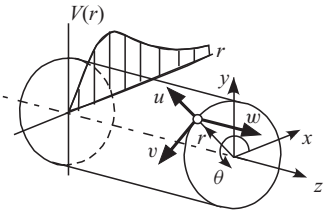


FIGURE 1. Schematic diagram of the mean flow and coordinate systems.

In order to understand the mechanisms of core fluctuation growth, we have previously studied the linear evolution of perturbations in an Oseen vortex (PH06). While the Oseen vortex is stable in terms of normal modes (i.e. modes with exponential behaviour in time), it supports substantial algebraic growth of perturbations that contribute vorticity outside the vortex core (Antkowiak & Brancher 2004, 2007). Perturbations that maximize energy amplification (i.e. 'optimal' modes) were seen to attain up to three-orders-of-magnitude amplification at moderate Re ($\sim 10^4$). In particular, bending wave optimal modes transiently grow through resonant excitation of core waves and generate large core perturbation energies (Antkowiak & Brancher 2004; PH06). These results may explain why bending waves are observed in turbulent vortex cores (Melander & Hussain 1993). The nonlinear evolution of these optimal modes could conceivably lead to core transition and sustained turbulence around the vortex, as in the case of other normal-mode-stable flows such as the plane Couette flow (Schmid & Henningson 2001). In the following, we use DNS to extend our linear analysis of Oseen vortex transient growth to the nonlinear regime.

Alternatively, one might formulate a nonlinear initial-value problem to find modes optimized for nonlinear growth (see Schmid & Henningson 2001 for an example of such a formulation). Nonlinear optimal modes need not coincide with linear optimal modes, as shown by Pringle & Kerswell (2010) for pipe flow. In the present case, however, we expect on physical grounds that nonlinear optimal modes will resemble the bending waves studied herein. This expectation is further supported by results in § 2.1, where it is shown that a vortex interacting with ambient turbulence develops bending waves that closely resemble linear optimal modes. Nevertheless, rigorous confirmation of nonlinear optimals is a worthwhile topic for future study.

2. Linear transient growth

Previously (Pradeep 2005; PH06), we analysed the linear-regime behaviour of arbitrary small-amplitude perturbations to the (normal-mode stable) Oseen vortex:

$$V = \left(1 - \mathrm{e}^{-r^2}\right)/r, \tag{2.1}$$

where V is the vortex's azimuthal velocity and r is the radius. In the following, we discuss the flow in both cylindrical coordinates (r, θ, z) with velocity components (u, v, w), and Cartesian coordinates (x, y, z), with velocity components (u_x, u_y, u_z). Primed quantities denote the three-dimensional fluctuation field and upper-case quantities the mean flow, obtained by averaging the field over θ and z. Figure 1 sketches the coordinate systems used.

The linear analysis was framed as an initial-value problem for perturbations of the form

$$\{u', v', w', p'\}(r, \theta, z, t) = \mathrm{Re}[\{\mathrm{i}\widetilde{u}, \widetilde{v}, \widetilde{w}, \widetilde{p}\}(r, t) \exp(\mathrm{i}m\theta + \mathrm{i}kz)], \tag{2.2}$$

https://doi.org/10.1017/jfm.2011.226 Published online by Cambridge University Press

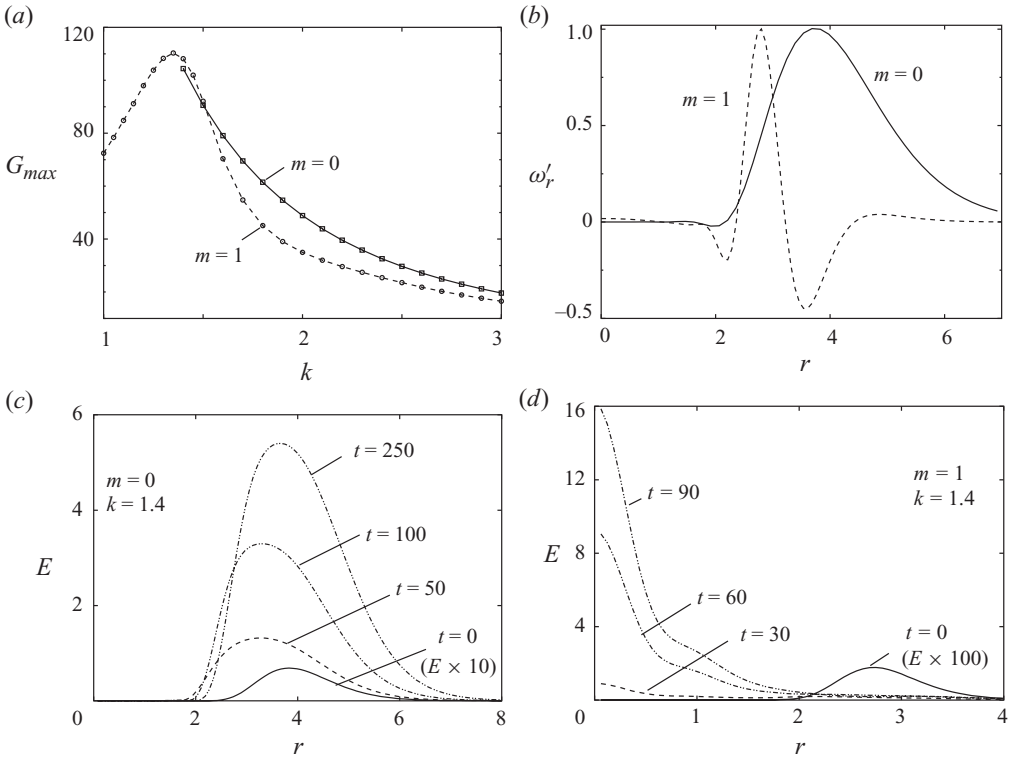


FIGURE 2. Results from linear analysis: (*a*) globally maximal gain $G_{max}(k)$ for $m = 0$ and $m = 1$; (*b*) initial ω_r' profiles for $m = 0$ and $m = 1$ global optimals at $k = 1.4$; (*c*) evolution of perturbation energy profiles $E(r)$ for $m = 0$ mode in (*b*); (*d*) $E(r)$ profiles for $m = 1$ mode in (*b*). In all cases, $Re = 5000$. Note that the initial ($t = 0$) perturbation plotted in (*c*, *d*) is magnified 10 times in (*c*) and 100 times in (*d*).

where u', v', w' are the radial, azimuthal and axial velocity perturbations and p' is the perturbation pressure, m and k are the azimuthal and axial wavenumbers, respectively, of the Fourier-decomposed perturbation. Note that unlike normal-mode stability analysis, no exponential-in-time behaviour is assumed. The linear analysis established that algebraically growing perturbations exist and extracted those perturbations ('optimal modes') which maximize energy amplification over a given time period of amplification t. 'Globally optimal' perturbations are defined as the optimal perturbations that maximize the amplification of perturbation energy, i.e. *gain* $G(t)$, over all t, for a given set of parameter values: m, k and Re; here Re is the vortex Reynolds number, defined as circulation/viscosity.

We now summarize some of the key results from linear transient growth analysis. Figure 2(*a*) shows the globally maximal gains $G_{max}(k)$ for axisymmetric ($m = 0$) and bending wave ($m = 1$) modes. G_{max} for $m = 0$ increases monotonically with decreasing k, attaining its largest value in the $k \to 0$ limit (consistent with decreased viscous dissipation at longer wavelengths). The largest-growing modes are, however, also found to be those with the smallest growth *rates*. Hence, peak amplification is attained at very large t. This is expected to limit the physical significance of these modes in vortex–turbulence interaction, where large-growth $m = 0$ modes can be overwhelmed by perturbations which reach nonlinear amplitudes earlier in the evolution (primarily $m = 0$ and $m = \pm 1$ modes). Figure 2(*b*) plots the initial radial perturbation vorticity ω_r' profiles for $m = 0$ and $m = 1$ global optimal perturbations at $k = 1.4$. The growth

https://doi.org/10.1017/jfm.2011.226 Published online by Cambridge University Press

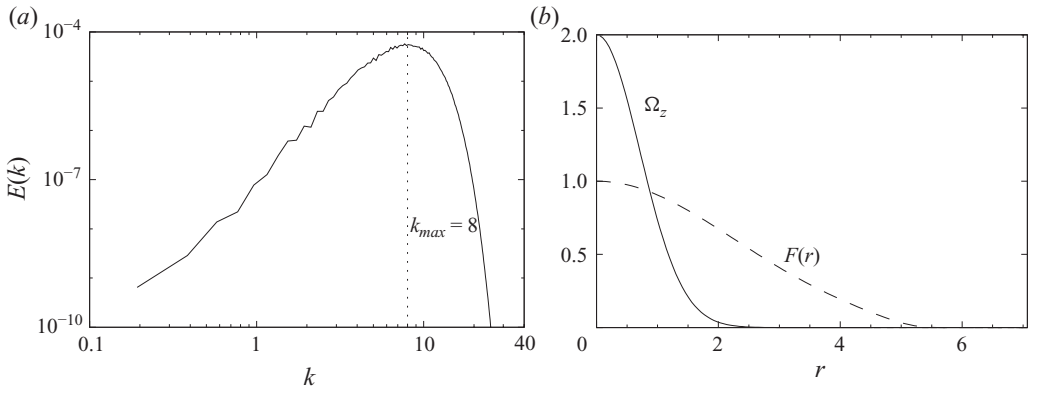


FIGURE 3. Definitions used for DNS of vortex–turbulence interaction at $Re = 5000$. (a) Initial perturbation energy spectrum using the Mansour & Wray (1994) spectrum with $k_{max} = 8$. (b) Profiles of the Oseen vortex mean axial vorticity, Ω_z, and the radial filtering function, $F(r)$, necessary for radial compactness.

mechanism involves the tilting of ω_r' to ω_θ' and concomitant vortex stretching; thus, for both modes, the azimuthal vorticity component is small at first compared to the radial and axial components, and is subsequently amplified via tilting and stretching. Note that the $m = 1$ mode is localized at smaller r than the axisymmetric mode. The Oseen vortex's mean strain rate outside the core increases with decreasing r, implying that the tilting and stretching of perturbation vorticity is faster for $m = 1$. This causes the bending wave modes to intensify faster than the axisymmetric mode, producing higher positive Reynolds stress, production and hence growth. With increasing Re, $m = 0$ modes migrate to progressively larger r (and have progressively decreasing growth rates due to decreased production), whereas $m = 1$ modes become increasingly localized at a single radius, where they resonantly excite a bending wave in the vortex core (PH06).

While for most k values, $m = 0$ modes have larger gains than $m = 1$ modes (figure 2a), the bending wave optimals possess two features that give these modes prime significance in vortex–turbulence interaction: first, as discussed previously, $m = 1$ modes feature large growth rates (compared to $m = 0$) and large gains (compared to $m > 1$ modes); second, bending wave modes grow through resonance with core waves, thereby exciting large fluctuations in the vortex core. This is seen in figure 2(d), where we plot the evolution of perturbation energy

$$E(r, t) = \frac{1}{4\pi L_z} \int \left(u'^2 + v'^2 + w'^2\right) \mathrm{d}\theta \, \mathrm{d}z$$

profiles. It can be seen the core fluctuations attain levels far exceeding the perturbation amplitudes outside the core ($r > 1$). In contrast, perturbation energy in $m = 0$ modes remains localized near the radial location of the initial perturbation (figure 2c). Thus, core transition (if it occurs) is likely to be the result of bending wave growth.

2.1. *Vortex–turbulence interaction*

In order to establish the relevance of transient growth during vortex–turbulence interaction, we consider the evolution of an Oseen vortex column embedded in initially fine-scale turbulence. The turbulence is numerically constructed as random fluctuations following the Mansour & Wray (1994) energy spectrum, shown in figure 3(a). The simulation uses the numerical method discussed in § 3. As the

https://doi.org/10.1017/jfm.2011.226 Published online by Cambridge University Press

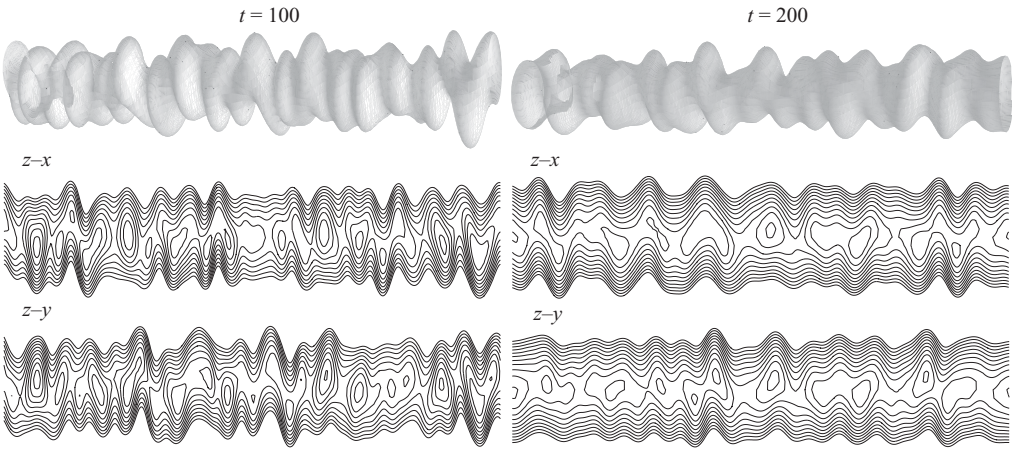


FIGURE 4. Vorticity magnitude surfaces (viewed looking at the column halfway – 45° – between $+x$ and $+y$ axes) for vortex–turbulence interaction at $Re = 5000$ showing core bending waves at $t = 100$ and $t = 200$. Vorticity magnitude contours are shown underneath in the z–x and z–y meridional planes (see figure 1 for axes). The vorticity contours begin at the outermost at $\omega = 1.2$ with step size $\delta\omega = 0.2$ and the vorticity surfaces match the third lowest contour level.

numerics require that the vorticity field vanish at the radial domain boundary, the turbulence is filtered in physical space by the function, $F(r)$, shown in figure 3(b). Results by Pradeep & Hussain (2004) show that for the domain sizes simulated herein the filtering has insignificant effect on the vortex column's evolution. The initial evolution of the fluctuation field – comprising pairing, vortex stretching and dipole formation – was examined in PH10. Here our focus is on the structure of core perturbations triggered by the 'ambient' turbulence.

The simulation considered here is at $Re = 5000$, and the flow is simulated in a domain size of $L_x \times L_y \times L_z = 10\sqrt{2} \times 10\sqrt{2} \times 14\pi$ using $192 \times 192 \times 512$ grid points. Turbulence intensity (ratio of r.m.s. velocity to peak mean velocity, v_1) is at 15 % and the energy spectrum has its maximum value at wavenumber $k = 8(\equiv k_{max})$, so that the characteristic length scale of the energy containing eddies is of the same order as the vortex core. As in PH10, we use a large initial turbulence intensity to offset the rapid initial dissipation, so that the fluctuations persist until late times.

Here, transient growth is not sufficiently strong to sustain the turbulence at its initial levels; hence, there is overall decay of three-dimensional energy. The decay is accompanied by the emergence of vortex core waves, as shown in prior numerical studies. The vorticity surfaces in figure 4 show that these waves are prominent by $t = 100$ and persist at a significant, though smaller, amplitude at later times.

The visualization shows the core waves excited by the turbulence. Views of the vorticity magnitude contours (figure 4) in two orthogonal meridional planes show that the waves are non-axisymmetric. The structure of the core fluctuations is complex, consisting of multiple axial wavelengths. It might appear that the dominant wavelength increases with time (compare $t = 100$ and $t = 200$), but in fact the evolution shown in figure 4 is the result of the growing relative dominance of a particular wavelength. This is revealed by the energy spectra plotted in figure 5, where we Fourier-decompose three-dimensional energy as a function of axial wavenumber k_z. As the total three-dimensional energy, E_{3D}, is a decaying function, figure 5 plots *normalized* three-dimensional energy $E(k_z, t)/E_{3D}(t)$ spectra to better reveal the preferential excitation of certain wavelengths within the core. We truncated the

https://doi.org/10.1017/jfm.2011.226 Published online by Cambridge University Press

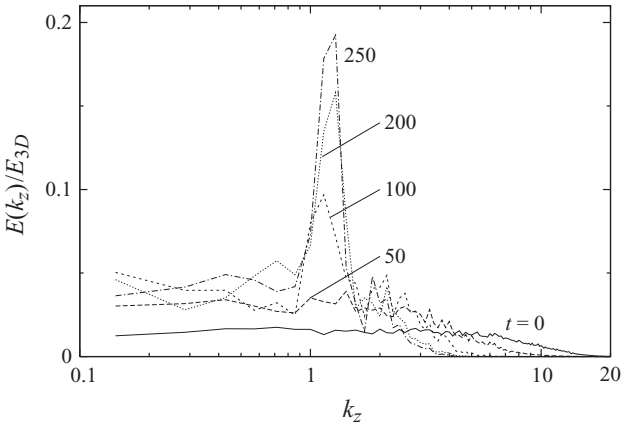


FIGURE 5. Normalized turbulent kinetic energy $E(k_z)/E_{3D}$ at different times.

fluctuating velocity field at $r>1$ for figure 5 so that the dominant modes within the core are captured. Outside the core ($r>1$), the stretching of azimuthal vorticity generates finer-scaled structures (i.e. increased energy at higher k_z), hence a broader energy spectrum. The initial condition distributes energy equally across a wide range of axial wavelengths, but after $t=50$ we observe the gradual emergence of a peak in the spectra. Wavenumbers between $k_z\approx 1$ and $k_z\approx 1.5$ dominate, with the peak located at $k_z\approx 1.1$ at early times ($t<200$) and at $k_z\approx 1.28$ at later times ($t>200$). For the axial discretization used in this simulation, the next larger wavenumber is $k_z=1.42$; we infer that the most excited modes are located in the range $1.1\leqslant k_z\leqslant 1.42$.

Figure 5 establishes that an intermediate range of wavelengths experience preferential excitation, or more precisely are better able to resist decay. That the dominant wavenumbers are not the largest ones permitted by the axial domain length may be used to infer that this is not merely the result of faster viscous decay at smaller wavelengths. We note that the dominant wavelengths are those for which linear transient growth theory predicts large gains for both $m=0$ and $m=1$. But the modes in figure 4 are bending waves, confirmed by visualizing the perturbation vorticity structure at $k=1.28$. Figure 6 plots ω_z' (figure 6*a–d*) in an axial plane and ω_y' in a meridional z–x plane (figure 6*e–h*, where it coincides with ω_θ') obtained by Fourier-decomposing the fluctuation field (here no radial filtering is applied). We see that the axial vorticity is initially unstructured at $t=50$, although an axisymmetric mode appears to be prominent within the core. Subsequent evolution of ω_z' shows that an azimuthal wavenumber $|m|=1$ structure dominates the core by $t=100$. Similarly, early ω_y' distribution at $t=50$ reveals a dominant axisymmetric component (ω_y' changes sign across the axis), which is replaced by a bending-wave-like structure at later times. The overall perturbation vorticity structure has strong qualitative resemblance to that obtained from the evolution of a single bending wave mode (see § 4.2 and figure 9). In particular, azimuthal vorticity is prominent outside the vortex core at late times (figure 6*f*, *g*) – necessary for transient growth and core wave excitation (PH06).

3. Numerical method

We simulate an isolated, temporally evolving vortex column periodic in the axial (z) direction (figure 1), using the method of Rennich & Lele (1997).

https://doi.org/10.1017/jfm.2011.226 Published online by Cambridge University Press

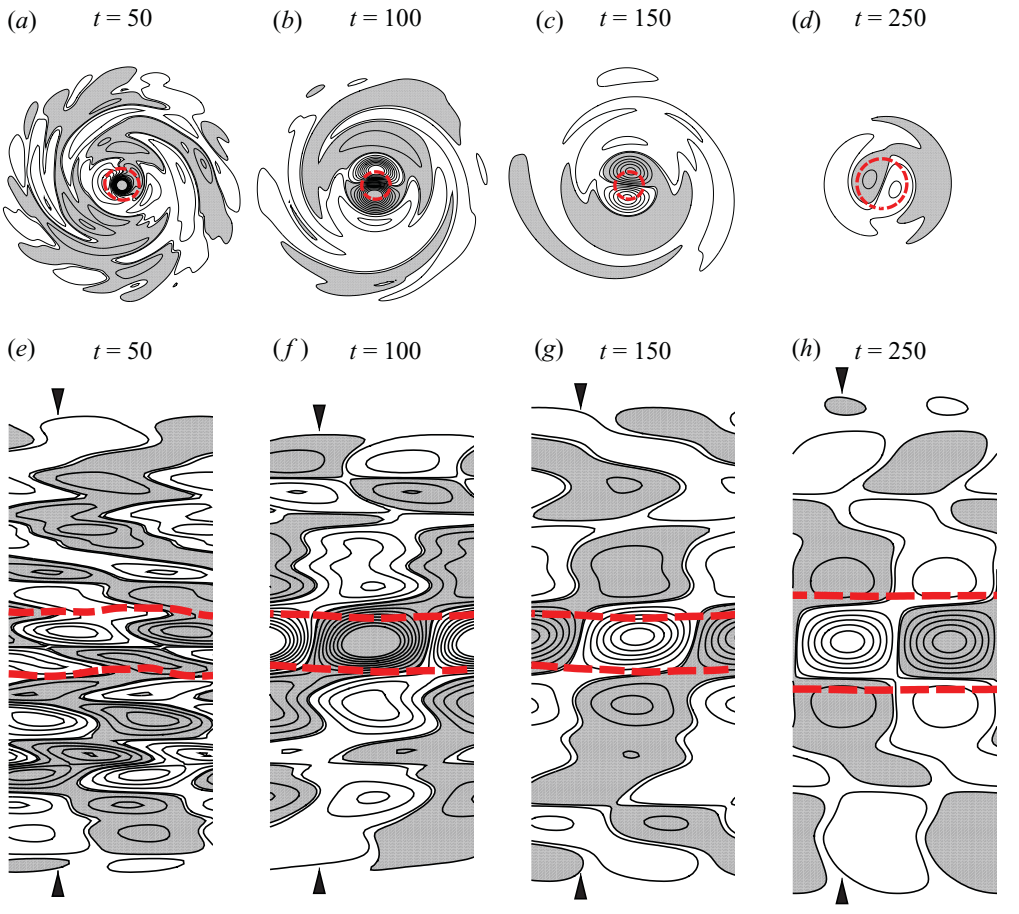


FIGURE 6. (Colour online available at journals.cambridge.org/flm) Contours of (*a–d*) ω_z' in an axial (x–y) plane, and (*e–h*) ω_y' in a meridional z–x plane – where it is coincident with ω_θ' – of only the $k_z = 1.28$ mode extracted from the fluctuation field. One axial wavelength of the $k_z = 1.28$ mode is shown in (*e–h*). Shaded regions contain negative-signed vorticity. The x–y plane is marked by arrows in (*e–h*). The lowest contour level is $|\omega| = 1 \times 10^{-8}$, with step size $|\delta\omega| = 1 \times 10^{-7}$, and the thick dashed contour at mean vorticity magnitude $\Omega = 1$ ($\Omega = 0.5$ at $t = 250$) denotes the vortex core.

The numerical scheme applies to flows with vorticity that is compact along the two unbounded directions (x and y). An initial vorticity field $\boldsymbol{\omega}$ is prescribed and the vorticity equation

$$\frac{\partial \boldsymbol{\omega}}{\partial t} + \nabla \times (\boldsymbol{\omega} \times \boldsymbol{u}) = \nu \nabla^2 \boldsymbol{\omega} \tag{3.1}$$

is integrated forward in time. This involves calculation of the induced velocity field $\boldsymbol{u}$. In the standard Fourier method, the (divergence-free) velocity field is obtained from the Fourier-transformed vorticity field, $\widetilde{\boldsymbol{u}}(\boldsymbol{k}) = \mathrm{i}\boldsymbol{k} \times \widetilde{\boldsymbol{\omega}}/k^2$ where tildes denote Fourier-transformed quantities and $\boldsymbol{k}$ is the wavevector. In addition to the velocity induced by vorticity within the computational domain, $\widetilde{\boldsymbol{u}}$ contains contributions from the infinite array of image flows in neighbouring domains in x and y.

To eliminate the influence of neighbouring domains, $\boldsymbol{u}$ is written as the sum of rotational and irrotational components: $\boldsymbol{u} = \boldsymbol{u}_\omega + \nabla\phi + \boldsymbol{U}$. Here $\boldsymbol{u}_\omega$ represents the

https://doi.org/10.1017/jfm.2011.226 Published online by Cambridge University Press

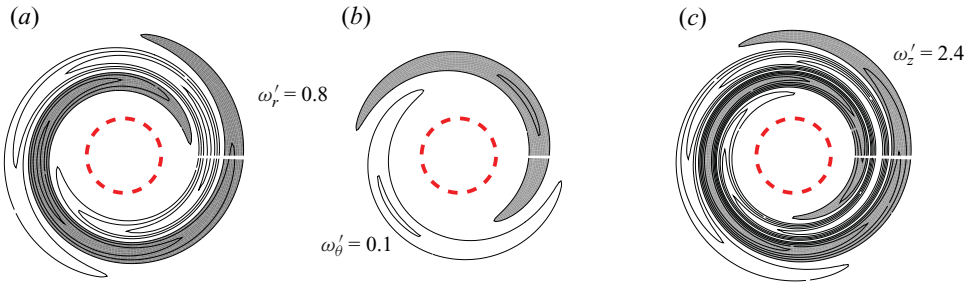


FIGURE 7. (Colour online) Perturbation vorticity contours of $m = 1$ and $k = 1.4$ optimal mode for $Re = 5000$ in a z-plane, with peak values indicated: (*a*) ω_r', (*b*) ω_θ' and (*c*) ω_z'. Inner circle is the mean vorticity $\Omega = 1$ contour and denotes the vortex core. Relative vorticity magnitudes are shown.

rotational part of the velocity, i.e. $\nabla \times \boldsymbol{u}_\omega = \boldsymbol{\omega}$; $\nabla\phi$ is the irrotational component of velocity, which ensures that the boundary conditions at $r \to \infty$ are satisfied; and $\boldsymbol{U}$ is the mean velocity, due to the $\boldsymbol{k} = 0$ component of the vorticity field. Each of these three components is solenoidal. The velocity potential ϕ satisfies $\nabla^2\phi = 0$, which is solved using the boundary conditions that ϕ is finite at $r = 0$ and as $r \to \infty$.

The numerical code has been implemented to run on parallel processors. All aspects of the algorithm are trivially parallelized, except the three-dimensional Fourier transforms. The computational domain is divided into equal slices along a coordinate direction and the slices are distributed across processors. Transforms in two directions are local and carried out first. The transform in the third direction is preceded by a global matrix transposition to render the data local.

Code validation has been discussed in Pradeep & Hussain (2004) and PH10.

4. Results

In the following, we discuss simulations initialized with a single optimal perturbation to a laminar vortex. We focus our attention on bending wave optimal modes ($m = 1$), which, for reasons discussed earlier, are likely to be the dominant modes during vortex–turbulence interaction. Consider four simulations (cases A–D), all initialized with the same optimal mode, with perturbation axial wavenumber $k = 1.4$. At $Re = 5000$, this mode produces maximum energy growth, peaking at time $t_{max} \approx 90$, with gain $G \approx 100$. Note that this is the globally optimal mode (figure 2*a*).

Initial vorticity component distributions obtained from linear analysis are plotted in one z-plane in figure 7. Note that the initial perturbation is dominated by the ω_z' and ω_r' components, and the vorticity is organized into spiral layers in the strain-dominated region ($r > 1$) of the mean flow. Here $\Omega = 1$ occurs at $r \approx 0.8$ (core radius), with the peak vorticity perturbation magnitudes of figure 7 occurring near $r \approx 2.4$ or three times the core radius. (The perturbation in figure 7 has been normalized to unit initial energy.) Perturbation energy in the linear regime grows through two mechanisms: (*a*) the tilting by the mean flow of ω_r' into ω_θ' and concomitant stretching of spiral vortex filaments (consequently, ω_θ' experiences rapid growth and generates significant positive $u'v'$); and (*b*) energy production because of the positive $u'v'$ Reynolds stress induced by the 'positive-tilt' spiral pattern of ω_z', where $+u'v'$ is necessary for energy growth.

We evaluate the effects of nonlinearity by initializing the same perturbation with different initial amplitudes (defined as the ratio of peak perturbation velocity u'_{max} to the peak mean azimuthal velocity v_1): 6.6×10^{-3} (case B), 2.1×10^{-2} (case C)

https://doi.org/10.1017/jfm.2011.226 Published online by Cambridge University Press

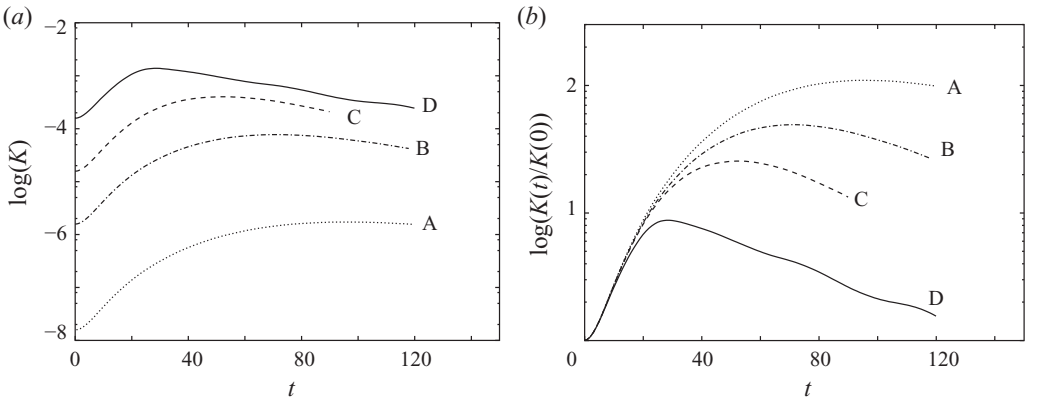


FIGURE 8. Energy evolutions at $Re = 5000$ for bending wave modes with increasing initial amplitudes – 0.066 % (case A, linear), 0.66 % (case B), 2.1 % (case C) and 6.6 % (case D): (*a*) $K(t)$, (*b*) $K(t)/K(0)$.

and 6.6×10^{-2} (case D). Case A is initialized with intensity 6.6×10^{-4}, but since flow evolution is obtained by solving the *linearized* Navier–Stokes equations, the numerical value of the intensity is irrelevant. The vortex column is specified by the velocity profile (2.1). It has peak vorticity (on the axis) of 2 and circulation $\Gamma_0 = 2\pi$. The maximum velocity $v_1 = 0.64$, this value being attained at the radius $r_1 = 1.12$.

All simulations are done at vortex Reynolds number $Re \equiv \Gamma_0/\nu = 5000$, where Γ_0 is the vortex circulation and ν is the kinematic viscosity. Computational domain size $L_x \times L_y \times L_z = 10\sqrt{2} \times 10\sqrt{2} \times 2\pi/1.4$ and all simulations use $512 \times 512 \times 128$ grid points.

4.1. *Effect of initial perturbation amplitude*

Figure 8(*a*) plots the evolutions of the volume-integrated perturbation energy

$$K(t) = \frac{1}{2} \int_{r=0}^{R} \int_{\theta=0}^{2\pi} \int_{z=0}^{L_z} \left(u'^2 + v'^2 + w'^2\right) \, r \, \mathrm{d}r \, \mathrm{d}\theta \, \mathrm{d}z, \tag{4.1}$$

where R is the domain size in the radial direction. (Note that $K(t)$ is the volume-integrated energy, whereas $E(r, t)$ is the profile of the energy averaged over θ and z.) It can be seen that with increasing initial perturbation intensity, the maximum energy amplification $G \equiv K(t_{max})/K(0)$ is progressively reduced. This is more clearly seen in figure 8(*b*), where we plot the normalized energies. All four cases have identical energy growths during early evolution ($t < 10$), showing that the initial growth is linear, as nonlinear self-interaction of the perturbation is small when ω'_θ is insignificant. There is approximately hundred-fold energy growth in linear evolution (case A), but barely ten-fold amplification in case D. (Note that the base flow is frozen in case A but freely evolves in cases B–D. The viscous decay of the base flow contributes to diminished growth in the latter cases, but the effect is expected to be weak at the fairly large Re considered here. Furthermore, the decrease in energy amplification across cases B–D establishes that nonlinear mechanisms contribute significantly to growth arrest.) The diminishing gain with increasing initial amplitude implies that there exists an optimal initial energy which maximizes peak perturbation energy for $t > 0$.

In addition to the gain G, the time period of growth is also progressively reduced with increasing initial intensity. The peak amplification time is reduced from $t_{max} = 90$ (case A) to $t_{max} = 30$ (case D).

https://doi.org/10.1017/jfm.2011.226 Published online by Cambridge University Press

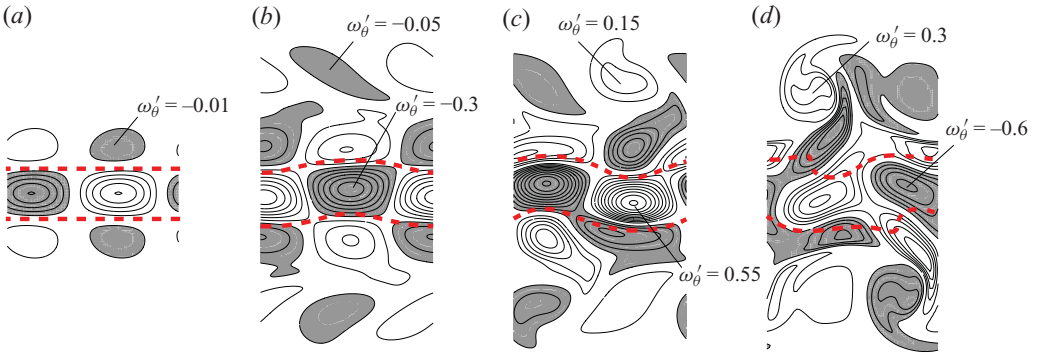


FIGURE 9. ω'_y contours in a meridional x–z plane at time of peak energy for various cases: (*a*) case A ($t_{max} = 90$), (*b*) case B ($t_{max} = 70$), (*c*) case C ($t_{max} = 50$) and (*d*) case D ($t_{max} = 30$). Maximal values of vorticity of the external fine-scale filament and core indicated. Shaded regions contain negative ω'_y. Total vorticity magnitude $\omega = 1$ contour (thick dashed) depicts the vortex core shape.

In the linear regime, growth is arrested through (*a*) the depletion of ω'_r through the induction of wave motion, and (*b*) the transformation of positive-tilt streamlines (producing positive Reynolds stress $\overline{u'v'}$) to negative-tilt streamlines (producing negative $\overline{u'v'}$) through the differential azimuthal advection of ω'_z by the mean swirl V (see PH06). Note, $\overline{u'v'}(r)$ is the θ- and z-averaged $u'v'$ profile. Growth arrest is further promoted by nonlinear effects, specifically the self-advection of perturbation vorticity.

To see this, consider perturbation vorticity distributions at times of peak energy amplification for the four cases. Figure 9 plots ω'_y in a meridional x–z plane; note that $\omega'_y = \omega'_\theta$ in the upper half-plane and $\omega'_y = -\omega'_\theta$ in the lower half-plane. The contours show how with increasing initial perturbation energy the vortex core is increasingly contorted, and vorticity magnitudes both within and outside the core are amplified. For case A (linear), the external vorticity has only one cell of appreciable magnitude, and vorticity distributions are sinusoidal in z. For cases B and C, the effects of nonlinearity are apparent in that z-variations are no longer perfectly sinuous. Furthermore, the external vorticity has two opposite-signed ω'_y cells along r. The vorticity cell at larger r results from the tilting of radial vorticity at the minima (at $r \approx 4$) in the initial ω'_r distribution (see figure 2*b*), whereas the cell at smaller r results from the maxima of the initial ω'_r distribution. Since the ω'_r values at these local extrema are of opposite sign, so is ω'_θ that is generated by the tilting of radial vorticity. For case D, the outer cell is in the process of rolling-up into a vortex filament ('thread') and its induced velocity appears to peel the inner vorticity cells away from the column. With further evolution (not shown), the two cells of opposite-signed ω'_θ form a vortex dipole, which self-advects radially outwards (away from the vortex column). Dipole motion will also transport residual ω'_r radially outwards, hence into regions of weaker mean strain rate. Transport of ω'_r into regions of weaker strain weakens the growth mechanism and contributes to the arrest of energy growth.

4.2. *Evolution of large-amplitude perturbation*

We now focus on case D, which has the largest initial perturbation amplitude. Mode evolution is shown in terms of vorticity contours in a meridional plane in figure 10 and in terms of vorticity isosurfaces in figure 11.

https://doi.org/10.1017/jfm.2011.226 Published online by Cambridge University Press

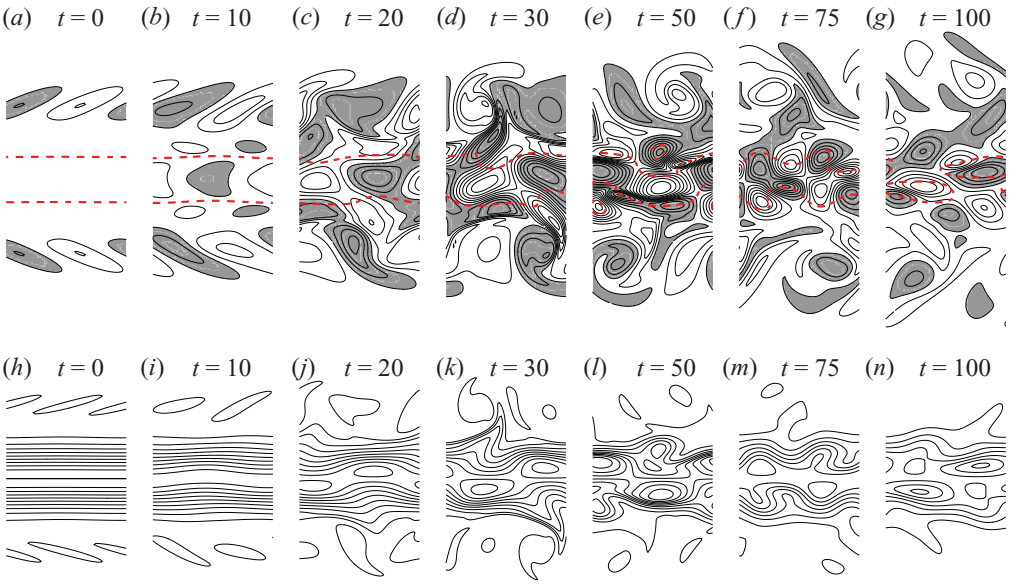


FIGURE 10. (Colour online) Contours of ω_y' (*a–g*) and total vorticity magnitude ω (*h–n*) in a meridional x–z plane for case D at $Re = 5000$. Shaded regions in (*a–g*) contain negative ω_y'. Contours plotted with increment $\delta\omega = 0.1$ in (*a–g*) and $\delta\omega = 0.2$ in (*h–n*). In (*a–g*) $\omega = 1$ contour (thick dashed) is also shown to indicate the vortex core.

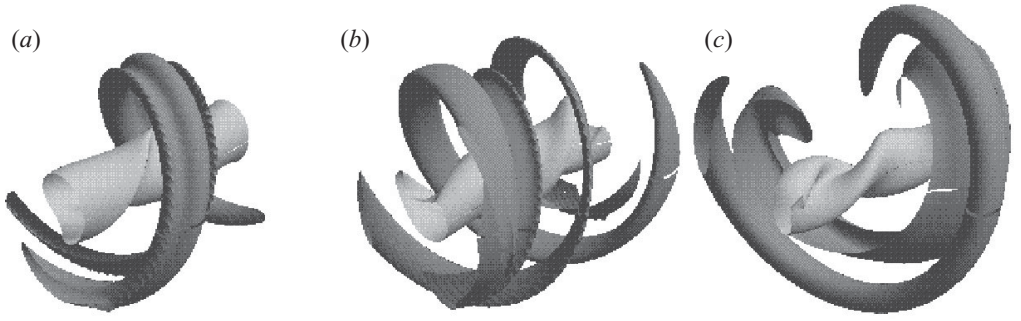


FIGURE 11. Isosurfaces of total vorticity magnitude ω for case D ($Re = 5000$) at (*a*) $t = 30$, (*b*) $t = 60$ and (*c*) $t = 90$. Light-shaded surfaces are $\omega = 1$ and depict the vortex column core; dark-shaded surfaces are $\omega = 0.3$ in (a, b) and $\omega = 0.15$ in (c) and depict the external vortex filament.

Initially, the vorticity perturbation is located only outside the core (figure 10*a*, *h*), with ω_θ' being small in comparison with ω_r' and ω_z' (figure 7). The strain field of the vortex column's swirl tilts ω_r' into ω_θ' and stretches the vorticity. The consequent growth of ω_θ' is seen in figure 10(*b–d*). The external vorticity is organized into a thread-like vortex filament (figure 11*a*). The optimal mode's external ω_θ' is localized at a radius where the thread's induced velocity perturbation in the column's core can resonate with a bending wave eigenmode of the Oseen vortex. The resonance leads to significant growth of core perturbation vorticity, whose magnitude soon exceeds that of the thread (figure 10*d*). Note that the bending wave is associated with nearly equal magnitudes in all three vorticity components. In the meridional x–z plane of figure 10, the growth of ω_r' (not shown) causes appreciable deflection of the vortex column's

https://doi.org/10.1017/jfm.2011.226 Published online by Cambridge University Press

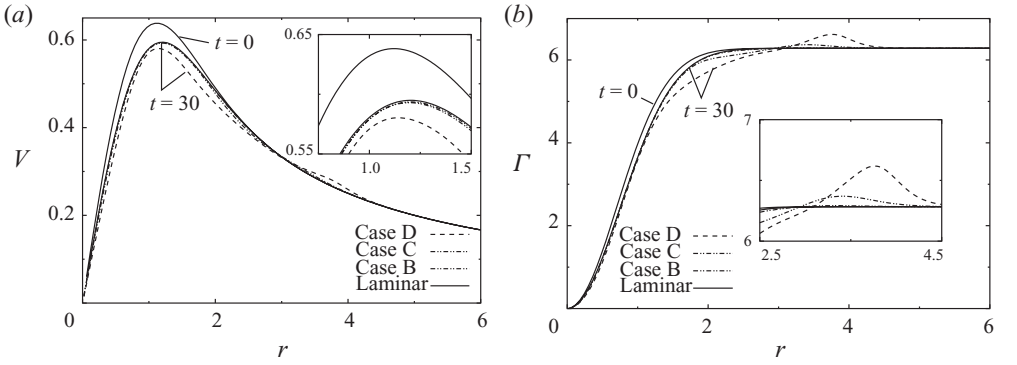


FIGURE 12. Profiles of (*a*) mean velocity V and (*b*) circulation Γ for cases B–D and the unperturbed laminar vortex; $Re = 5000$. v_1 is peak azimuthal velocity.

axis; the deformation of the initially rectilinear column into a helical bending wave can be discerned in figure 10(d, k), and more clearly in figure 11(a, b).

The preceding mechanisms are essentially linear, but nonlinear effects strengthen progressively and are clear at larger times, $t > 30$. (See also the deviation of energy evolution from linear growth in figure 8b, at these times.) The most significant nonlinear effect is the roll-up of the external vorticity patches – of the type seen in figure 9(a) – into threads, evident in figure 9(d). The self-induced motion of each segment of the spiral vortex filament (figure 9b) advects the segment axially (along z). (The apparent movement of the threads in the z-direction in figure 10 is due to both the thread's self-induced motion along the column as well as the azimuthal advection of the spiralling perturbation by the mean swirl.) Furthermore, the weaker ω'_θ cell located initially at smaller r is wrapped around the stronger ω'_θ cell (figure 10d). The detailed vortex dynamics of these vortex filaments is complex, but the net effect of the self-induced motions of the threads (negligible in the linear limit) is that opposite-signed cells are organized into dipole-like structures. The mutually induced motions within the dipole carry the dipole radially outwards. Such radially outward motion of the external filaments is clearly seen by comparing figure 10(c, g), and more clearly in the isosurfaces in figure 11(a, c). The cumulative effect of transient growth is that flow appears to be nearly turbulent at late times. While no core transition is observed in the present case, the isosurfaces in figure 11(c) show the significant distortion of the column.

4.3. *Flow statistics*

The growth of a single optimal perturbation qualitatively reproduces the main statistical features observed in the case of a vortex interacting with fully developed turbulence. These include (*a*) the development of a mean circulation overshoot, (*b*) enhanced decay of mean azimuthal velocity and (*c*) development of intense core fluctuations.

The decay of the mean azimuthal velocity V is shown in figure 12(a) for a laminar vortex column and cases B–D at $t = 30$. For the two lower-intensity cases, the mean flow profiles are nearly indistinguishable from the laminar case, but case D shows appreciably faster decay. What is interesting is that the radial location r_1 of azimuthal velocity peak shifts radially *inwards* with increasing initial perturbation intensity (see inset). This enigmatic effect of turbulence on mean core radius has also been observed in experiments (Bailey & Tavoularis 2008) and deserves further study.

https://doi.org/10.1017/jfm.2011.226 Published online by Cambridge University Press

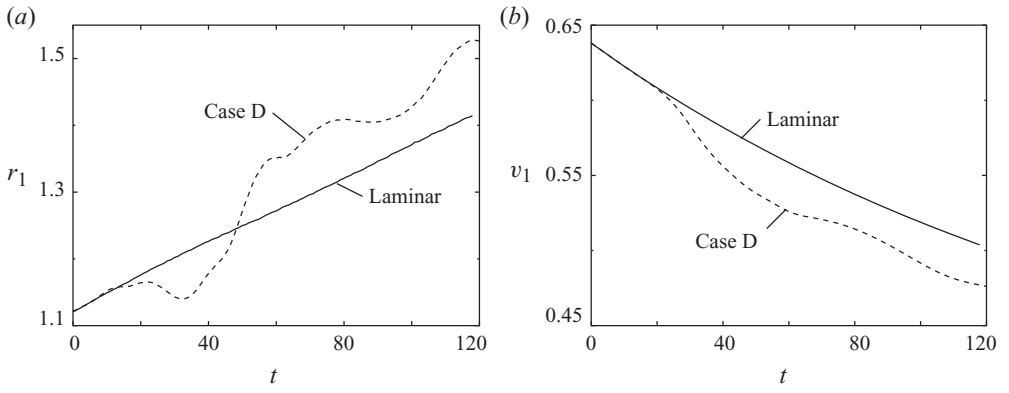


FIGURE 13. Evolution of (a) core radius r_1 and (b) peak azimuthal velocity v_1 for case D, compared with evolutions for the corresponding laminar vortex (both at $Re = 5000$).

The decay of peak mean velocity v_1 and the growth of the core radius r_1 are more clearly seen in figure 13, where we compare case D with laminar vortex evolution. The evolution of both these quantities is substantially affected by the perturbation. Our previous DNS results (PH10) of vortex–turbulence interaction showed significantly weaker decay, even at higher Re (12 500). For instance, while r_1 for case D is approximately 16 % higher than the laminar flow, randomly initialized turbulence showed only a 2 % enhancement. It is possible that the selection of a large peak k for the initial energy spectrum in PH10 failed to excite the bending wave optimal mode. The comparison indicates the sensitivity of mean flow evolution to the initial conditions. In experimental flows, ambient turbulence may well excite optimal modes and accelerate vortex decay.

Consistent with the faster-than-viscous decay of mean velocity in case D, the mean circulation profiles display an overshoot (figure 12b). The overshoot magnitude at $t = 30$ is approximately 6 % for case D, and would increase with increasing initial fluctuation intensity. The Re trend of overshoot magnitude has not been investigated here, but it is expected that the overshoot will increase with increasing Re as well – due to both the increased magnitude of transient growth and the weakened cross-diffusion within the thread dipoles responsible for the overshoot.

We now turn to some basic statistics of the fluctuation field. The profiles of the turbulence intensity $\widehat{u}$, defined as

$$\widehat{u}^2 = \frac{1}{2\pi L_z} \int_{\theta=0}^{2\pi} \int_{z=0}^{L_z} \left(u'^2 + v'^2 + w'^2\right)\, r \,\mathrm{d}\theta \,\mathrm{d}z, \tag{4.2}$$

normalized by the mean velocity scale v_1 are shown in figure 14(a). The initial fluctuations are localized around $r \approx 2.5$ and have an intensity of $\approx 6\,\%$. Optimal mode growth leads initially to the growth of fluctuations both within and outside the vortex core ($0 < t < 30$). Core fluctuations become very intense, attaining levels as high as 40 %. The growth of external fluctuations is associated with the generation of ω'_θ. Azimuthally oriented vortex filaments (see e.g. figure 10d) induce u' and w'. The radial motions due to u' advect the mean azimuthal momentum; note that advection by both positive and negative u' results in positive $u'v'$ – the stress component which must be positive for turbulence production to occur.

Thus, the Reynolds stress $\overline{u'v'}$ (figure 14b), which is initially small everywhere, exhibits large growth (see $t = 10$ profile). This growth is nearly the same as in linear

https://doi.org/10.1017/jfm.2011.226 Published online by Cambridge University Press

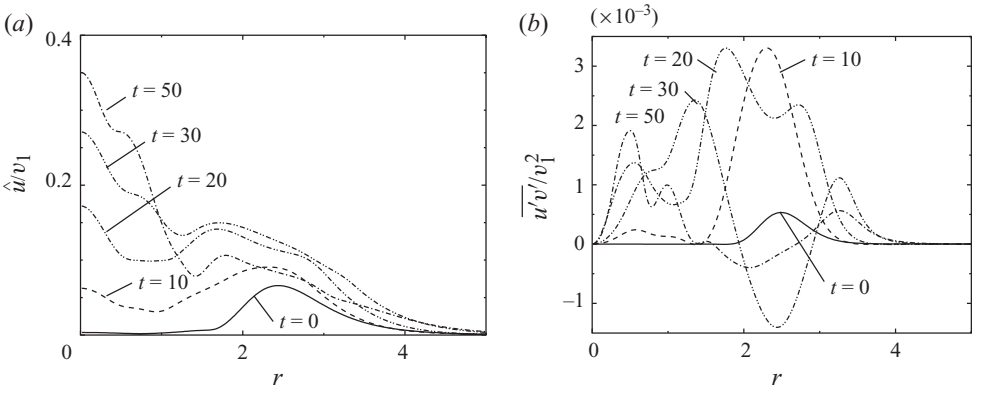


FIGURE 14. Evolution of normalized turbulence intensity (*a*) $\widehat{u}/v_1$ profiles and (*b*) normalized Reynolds stress $\overline{u'v'}/v_1^2$ profiles for case D at $Re = 5000$.

transient growth. At later times ($t = 20$), the $\overline{u'v'}$ stress at the radial location of its initial peak begins to decay, but two secondary peaks appear at larger and smaller radii. These peaks are associated with the two secondary cells of opposite-signed ω'_θ seen in figure 10(*c*). Further evolution of the stress is complex, exhibiting oscillatory dynamics at fixed r: see for instance the reversal of $\overline{u'v'}$ sign at the initial peak stress location (where the stress becomes negative at $t = 30$ and starts to decrease to zero at $t = 50$). Such oscillatory behaviour is probably the result of wave-like motions induced by the effect of residual mean vorticity outside the vortex core, as in the case of linear transient growth.

What is interesting is that the core fluctuations continue to amplify even after the external turbulence starts to decay (see $t = 50$ profile in figure 14*a*). This behaviour has also been observed in vortex–turbulence interaction and can be understood in terms of the resonant excitation of the bending wave in the core. Even as the external threads decay, they continue to induce velocity perturbations within the core (although the perturbation amplitude decreases with time). The tilting of mean vorticity in the core continues to feed the growth of the bending wave – because of resonance. Core perturbations do not grow indefinitely; at later times ($t > 50$, not shown), the core perturbations also decay. In addition to viscous effects (i.e. stronger damping of core perturbations relative to the inviscid forcing of the wave by the weakening external perturbation), inviscid 'detuning' of resonant core wave forcing may also contribute to core perturbation decay. That is, as the external filaments migrate to larger r through nonlinear self-advection, they are no longer located at the 'resonant radius' (PH06) where strong transient growth is possible.

The profiles of r.m.s. vorticity fluctuations (figure 15) qualitatively verify the basic mechanisms of transient growth and decay, discussed above. The radial vorticity fluctuations (see the inset of figure 15*a*) are initially located outside the vortex core and progressively decrease with time. The azimuthal vorticity fluctuations exhibit strong growth, through the tilting and stretching effect of the mean strain. The resonant excitation of the bending wave in the core leads to strong growth of both vorticity components (see profiles at $r < 1$). The radial oscillations of ω'_θ at late times ($t = 50$) are the result of the complex vorticity field structure (see e.g. figure 10*f*), comprising many thread-like structures with predominantly azimuthal vorticity.

https://doi.org/10.1017/jfm.2011.226 Published online by Cambridge University Press

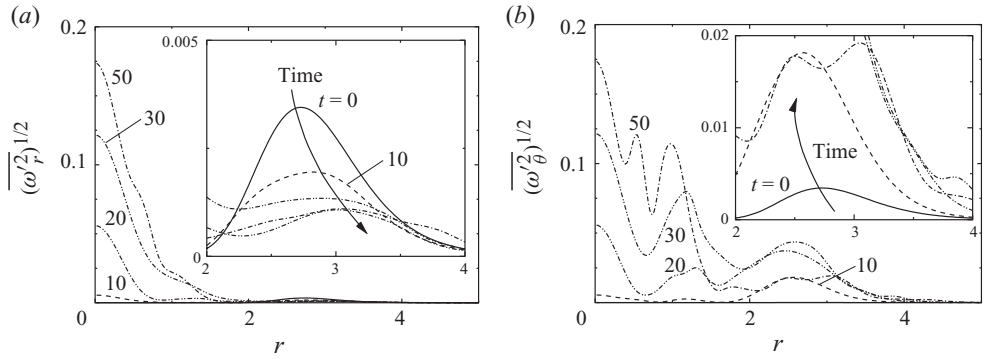


FIGURE 15. Evolution of r.m.s. (*a*) ω_r' and (*b*) ω_θ' profiles for case D at $Re = 5000$. Insets show a zoomed-in view near the radius of the initial perturbation peak.

In summary, the varying initial amplitude cases at fixed Re, A–D, show that an increase in initial perturbation amplitude results in an increase in complexity of the evolved flow. The large-amplitude case D, in particular, reproduces features of vortex interaction with developed turbulence. To further establish the relevance of transient growth in practical flows, we now explore the effects of increasing Re.

4.4. *Effects of Re*

While typical practical Re ($\sim 10^6$) are inaccessible for study via DNS, insights into the dependence on Re of the evolution of optimal modes can be obtained by comparing simulations with similar initial conditions at different Re. In this section we compare three simulations, at $Re = 2000$, 5000 and 10 000. Again, the initial conditions are the corresponding globally optimal bending wave at each Re (for $m = 1$ and $k = 1.4$). To focus on the turbulent-like state resulting from nonlinear transient growth, the initial amplitude is increased to 6 %.

As the initial perturbation field is obtained by solving the *viscous* linear stability problem (see PH06 for details), the optimal perturbation field is a function of Re, and the three initial conditions have subtle differences. All three initial conditions feature spiral layers of vorticity dominated by the ω_r' and ω_z' components, as seen in figure 7 for the $Re = 5000$ optimal mode. The radial location of the spirals is determined by the optimal mode selection process to be such that vorticity is localized around the critical radius where there is resonant interaction with a vortex (PH06). At a given Re, the radial width of the spiral is set by a balance between competing effects: localization of vorticity promotes resonance, whereas a broader spatial distribution of vorticity mitigates viscous cross-diffusion of opposite-signed vorticity that is present in spiral layers adjacent to the vorticity peak seen in figure 7 (these bands are not visible in figure 17 at $t = 0$ due to the contour levels). With increasing Re, perturbations with more concentrated spiral vorticity patterns are selected as optimal. This variation of the optimal initial condition with Re is clearly seen in figure 17.

Energy evolutions for the three Re cases are shown in figure 16, and figure 17 provides flow visualizations. While there is little variation of peak energy amplification with Re, the decay of perturbation energy is slower with increasing Re (figure 16). The fine-scale structures (threads) seen in figure 17 are generated through the inviscid processes of ω_θ' stretching, collapse of perturbation vorticity patches into fine-scale vortex threads, and self- and mutually induced motions of these threads. Viscosity is expected only to set the equilibrium scale of threads (as in the Burger's vortex) and to

https://doi.org/10.1017/jfm.2011.226 Published online by Cambridge University Press

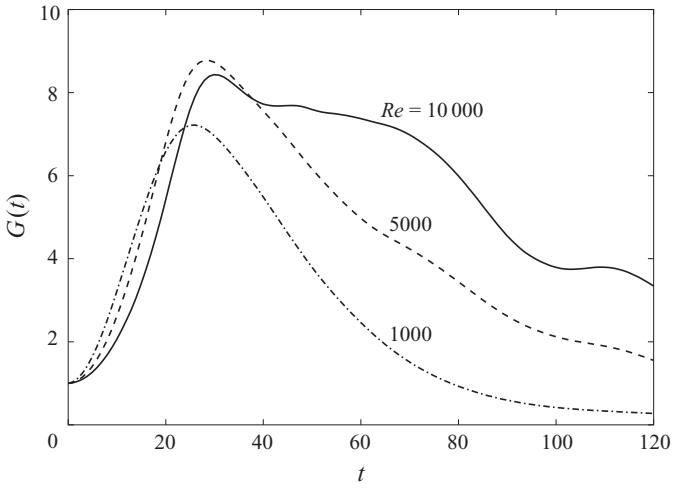


FIGURE 16. Perturbation energy evolution for global optimal modes of each Re with 6 % initial amplitude.

govern the rate at which they decay through dissipation and viscous cross-diffusion. Indeed, different Re values show a similar pattern of threads (figure 17), especially at the two higher Re, and several threads at $Re = 5000$ have clearly identifiable counterparts at $Re = 10\,000$. Thus, while equally energetic threads are generated at $Re = 2000$ and $Re = 10\,000$, those at the higher Re survive longer against weakened viscous damping.

Figure 17 shows increasing distortion with Re of the vortex column's core as a result of transient growth. The large-amplitude bending wave on the core is depicted by the $\omega = 1$ contour in figure 17(d). Initial evolutions (during the energy growth phase) are similar for all Re. At later times ($t = 100$), the lowest Re flow is rendered nearly laminar by viscous damping, whereas the highest Re case persists in resembling a turbulent flow. With increasing Re, the flow becomes more complex, featuring finer threads with larger peak vorticities. This is the expected result of threads undergoing vortical interactions such as mutually induced advection, pairing, tearing and reconnection. These interactions also result in a wider radial dispersal of the 'turbulence' with increasing Re due to thread dipoles surviving for longer times. Note that flow evolution towards a turbulent-like state persists after peak perturbation energy levels have been attained: figure 16 shows that perturbation energy starts to decay after $t \sim 30$, although the $Re = 10\,000$ flow is progressing towards greater structural complexity even at $t = 100$ (see figure 17o).

The $Re = 10\,000$ energy evolution (figure 16) shows that perturbation energy tends towards a plateau during the decay phase, starting at $t \approx 40$; there is even a brief period of renewed energy amplification at $t \approx 110$. This naturally raises the question as to whether transient growth can trigger sustained turbulence at high Re, perhaps through 'regenerative' transient growth. We note that an analogous mechanism of sustained turbulence has been found in boundary layers through regenerative transient growth (see Schoppa & Hussain 2002).

To explore this possibility in a 'cleaner' flow, we now consider the $Re = 10\,000$ flow at a reduced initial amplitude of ≈ 2 %. Figure 18, plotting the energy evolution at this reduced amplitude, clearly reveals a second phase of transient growth around $t = 150$. This weak, albeit distinct, regenerative energy growth is evidently nonlinear in origin

https://doi.org/10.1017/jfm.2011.226 Published online by Cambridge University Press

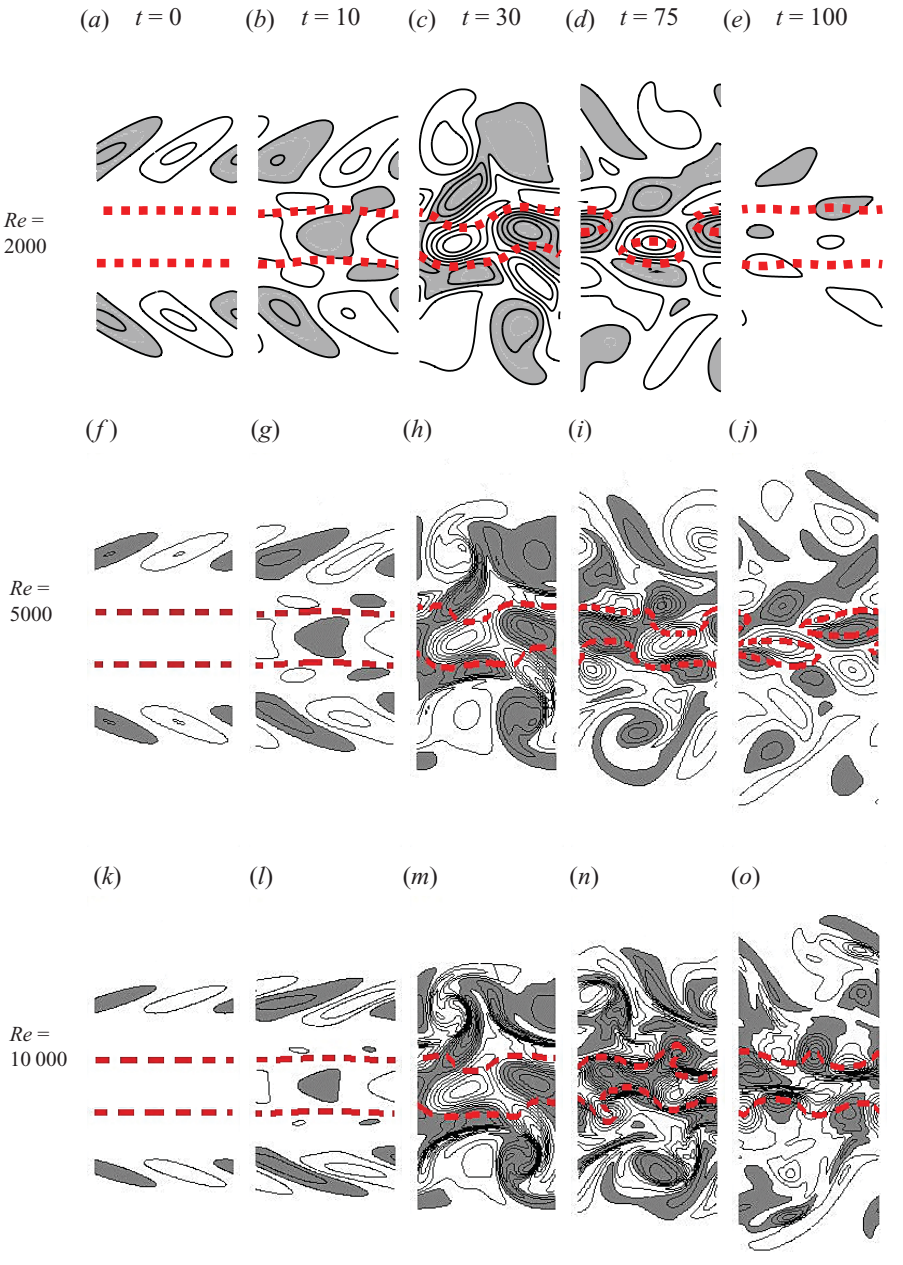


FIGURE 17. (Colour online) Contours of ω_y' in a meridional x–z plane for the global optimal modes. Shaded regions in (a–o) contain negative ω_y' and $\omega = 1$ (thick dashed contour) indicates the vortex core.

as it finds no counterpart in the corresponding linear-regime evolution plotted in the same figure.

To understand the physics of regenerative growth, we examine the vortex dynamics during the secondary growth phase (figure 19): ω_y' contours are plotted in a meridional

https://doi.org/10.1017/jfm.2011.226 Published online by Cambridge University Press

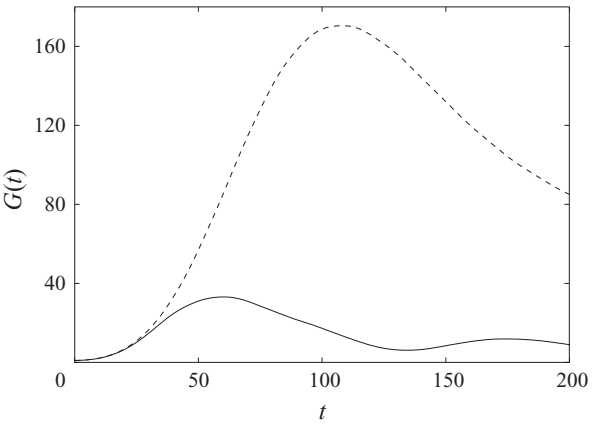


FIGURE 18. Perturbation energy evolution of the global optimal mode at $Re = 10\,000$ for a 2 % (solid line) initial amplitude and the linear energy evolution (dashed line).

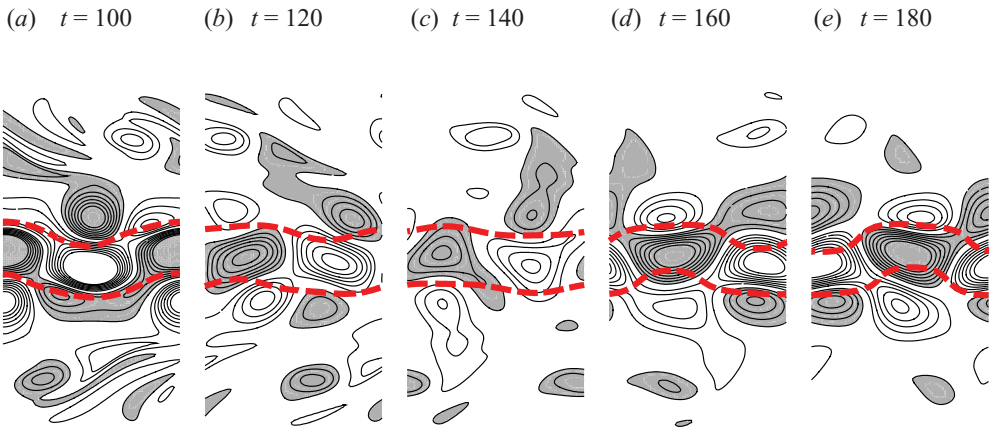


FIGURE 19. (Colour online) (*a–e*) Contours of ω_y' in a meridional x–z plane for the global optimal mode at $Re = 10\,000$ with 2 % initial amplitude. Shaded regions contain negative ω_y' and $\omega = 1$ contour (thick dashed) indicates the vortex core.

x–z plane, where $+\omega_y'$ coincides with $+\omega_\theta'$ in the upper ($+x$) half-plane. The evolution captures both the energy decay phase ($t = 100$ to $t = 140$) and the secondary growth phase ($t = 140$ to $t = 180$). All panels are plotted with the same contour levels. At $t = 100$, there are relatively intense structures at the core periphery. These gradually decay and by $t = 140$ are approximately fourfold weaker (in terms of circulation) than at $t = 100$. By $t = 140$, there is very little thread vorticity in the immediate vicinity of the core. Consequently, vorticity perturbations inside the core also appear to decay (compare vorticity at the axis at $t = 100$ and $t = 140$). At $t = 160$, however, ω_θ' reappears outside the core and is further intensified everywhere at $t = 180$. Thus, energy amplification (figure 18) and ω_θ' amplification are coincident. This is not surprising because ω_θ' dominated threads induce velocity perturbations which generate $+u'v'$ Reynolds stress, hence production. The resemblance of this process to the mechanism of the first phase of transient growth is, however, striking – indicating a similarity in the physical mechanisms that drive the initial and secondary growths.

https://doi.org/10.1017/jfm.2011.226 Published online by Cambridge University Press

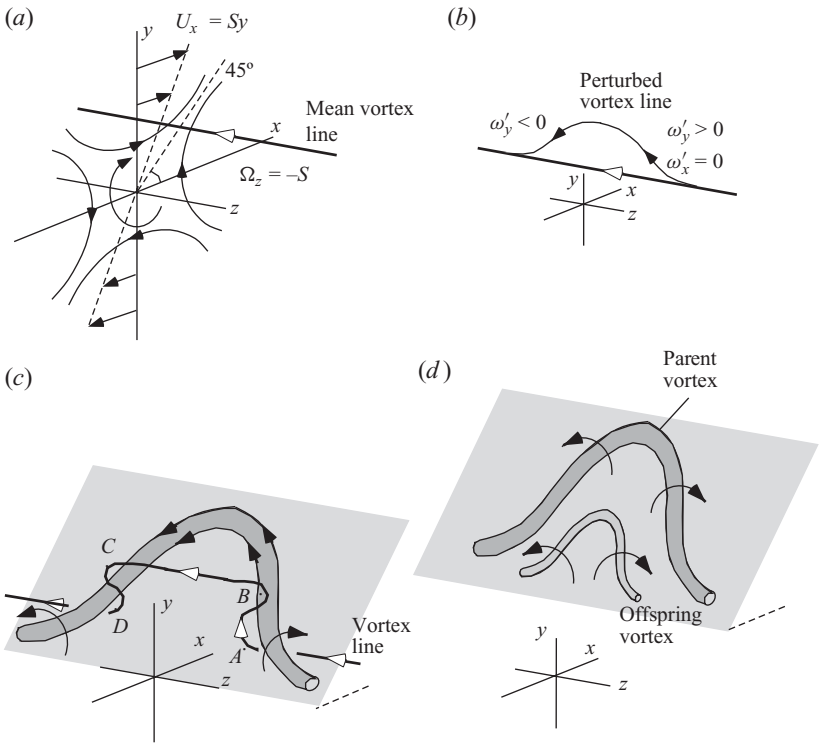


FIGURE 20. Schematic diagram of perturbation evolution in homogeneous shear flow.

Recall that optimal bending wave perturbations are characterized by predominantly radial vorticity at $t = 0$. If secondary growth occurs through a similar physical mechanism, it is necessary for ω_r' to be regenerated at the core periphery. In the following sections, we explore a possible mechanism of ω_r' regeneration and study regenerative transient growth in greater detail.

4.5. *Regenerative growth*

We present some arguments here of how self-sustained turbulence may occur through regenerative transient growth. A mechanism analogous to that in plane shear flow might be operative, as supported by observations of vortex optimal mode growth presented in the following.

Consider briefly perturbation evolution in plane homogeneous shear flow. The process is shown schematically in figure 20 and is based on results from the DNS study of Kida & Tanaka (1994). The mean flow has only streamwise velocity and is assumed linear, $U_x = Sy$ (figure 20*a*). The shear can be decomposed into a solid-body rotation ($U_x = Sy/2$, $U_y = -Sx/2$) with vorticity $\Omega_z = -S$ and pure straining motion ($U_x = Sy/2$, $U_y = Sx/2$). The principal axis of stretching (compression) is inclined at 45° (−45°) to the streamwise direction. Thus, a perturbation vorticity vector in the vertical direction y is tilted towards the principal stretching direction (thereby also generating streamwise vorticity ω_x') and experiences growth of vorticity magnitude. The mean vortex lines run along the negative z (spanwise) direction.

Now consider what happens when the vortex lines are given a spanwise-varying perturbation with non-zero ω_y' and zero ω_x' and ω_z'. Such a vortex line is shown in figure 20(*b*). The crest, being at larger y than the remainder, is advected faster along

https://doi.org/10.1017/jfm.2011.226 Published online by Cambridge University Press

x by the mean flow; hence, the length of the vortex line and perturbation vorticity magnitude grow (i.e. vortex stretching). Note that this process also generates ω_x', as the principal stretching direction is inclined at 45° to the streamwise direction. Perturbation vorticity is preferentially stretched along this direction, thus generating both ω_x' and ω_y'. The stretching process will continue indefinitely so long as $\omega_y' \neq 0$. With increasing amplitude of perturbation vorticity, a fine-scale vortex 'hairpin' is generated, with local swirl around the fine-scale vortex filament (figure 20*c*). The induced velocity of the hairpin vortex wraps the mean flow vortex lines around the vortex core and stretches ω_z' between the legs of the hairpin; i.e. the vortex line segment BC in figure 20(*c*) is stretched. Simultaneously, this wrapping process generates new ω_y': segments AB and CD in the figure. The new, perturbed vortex lines have geometry similar to the original perturbed vortex lines (figure 20*b*) and undergo similar stretching. The result is a new hairpin vortex, upstream of the original vortex. Note that the 'parent' hairpin is still present while the 'offspring' undergoes a similar evolution; thus, the mechanism of hairpin vortex formation can remain qualitatively similar for successive generations. This 'parent–offspring' scenario is proposed for structure regeneration and turbulence self-sustenance in the boundary layer (Smith & Walker 1995; Zhou *et al.* 1999).

A substantially similar process (figure 21) may occur outside the core of the Oseen vortex as well. Figure 21(*a*) shows a perturbed vortex line, obtained by introducing axially varying ω_r' (as well as ω_z' to satisfy divergence free-ness), with ω_θ' remaining zero. (Note that the mean vorticity Ω_z, while weak, is non-zero outside the core of the Oseen vortex.) Such a perturbation is similar to the vorticity of the optimal modes (see e.g. ω_θ' outside the core in figure 10*b* which would be generated by the initial ω_r'). As in the case of plane shear flow, the mean strain field tilts and stretches the perturbation vorticity, in this case generating and amplifying ω_θ'. The amplification will continue as long as $\omega_r' \neq 0$. This process results in a hairpin-like thread, wrapping around the vortex core (figure 21*b*). There are important differences between the hairpin vortex of the plane shear flow and the thread of the vortex flow. First, each leg of the thread (segments AB and AC) has significant curvature, whereas the shear-flow hairpin legs lie roughly in one (inclined) plane. The curvature implies self-induced motion (along z) of each of the segments AB and AC – similar to the self-induced motion of a vortex ring. For the specific initial perturbation of figure 21(*a*), these self-induced motions cause the two legs to approach each other. Second, the mutual induction of each leg on the other causes the entire thread to be advected radially outwards (figure 21*c*) to regions of decreasing strain. As mean strain rate decreases like $1/r$, threads will not be able to maintain themselves indefinitely against viscous cross-diffusion, which progressively increases as the individual legs come closer to each other. Nevertheless, before the thread decays, it can generate an offspring vortex through a process similar to that in the plane shear flow case. The legs of the threads wrap the mean vorticity around the thread core, as seen in figure 21(*b*). This process generates new ω_r' and also stretches the axial vorticity, producing ω_z'. Stretching and tilting of ω_r' generate a new (offspring) thread (figure 21*c*), oriented oppositely to the parent vortex.

Note that the inviscid mechanisms depicted in figures 20 and 21 will be tempered by viscous diffusion.

4.6. *Regenerative mechanism simulation*

The feasibility of this regenerative mechanism is supported by an idealized simulation starting with the initial condition sketched in figure 21(*a*). Consider an initial condition

https://doi.org/10.1017/jfm.2011.226 Published online by Cambridge University Press

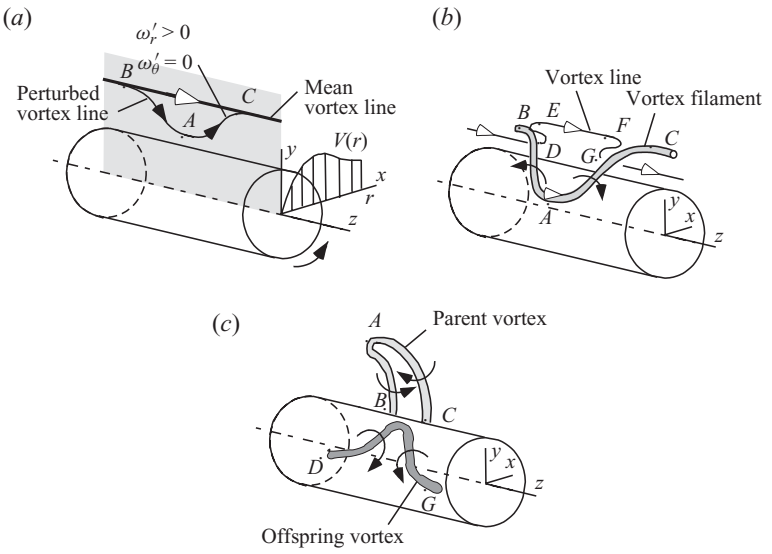


FIGURE 21. Postulated turbulence self-sustenance mechanism in the Oseen vortex.

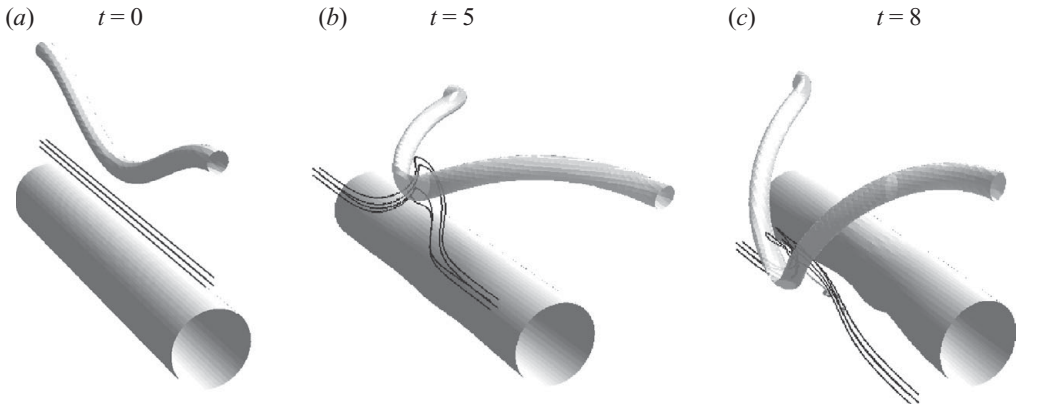


FIGURE 22. Visualization of the DNS result depicting time evolution of hairpin regeneration mechanism at $Re = 10\,000$. Two vorticity magnitude surfaces capture the vortex column ($\omega = 1.75$) and the parent vortex thread ($\omega = 2$). Vortex lines corresponding to the offspring thread are also captured.

comprising a curved vortex filament parallel with the column (figure 22); this idealized simulation is performed at $Re = 10\,000$. The perturbed vortex tube represents the parent thread, and the lines are vortex lines in the induced offspring thread. Flow evolution is also visualized by ω_r' and ω_θ' contours in a meridional plane (figure 23).

The parent thread initially contains radial and axial vorticity components only (ω_r' shown in figure 23*a* and ω_z' maintains divergence free-ness), like the perturbed vortex line in figure 21(*a*). As the thread is swirled by the vortex column, ω_θ' is generated in each leg of the hairpin thread ($t = 3$, figure 23*b*). The column's strain field deforms the parent thread's core into an elliptical shape, but this does not significantly alter the induced velocity field. The swirl induced by the parent thread's ω_θ' tilts the mean (axial) vortex lines, generating new ω_r' underneath the initial hairpin (figure 23*a*). This new ω_r' is oriented oppositely to the parent thread's initial ω_r', as also shown in figure 21(*a*, *b*). The bundle of vortex lines in figure 22(*b*, *c*) depicts the tilted vortex

https://doi.org/10.1017/jfm.2011.226 Published online by Cambridge University Press

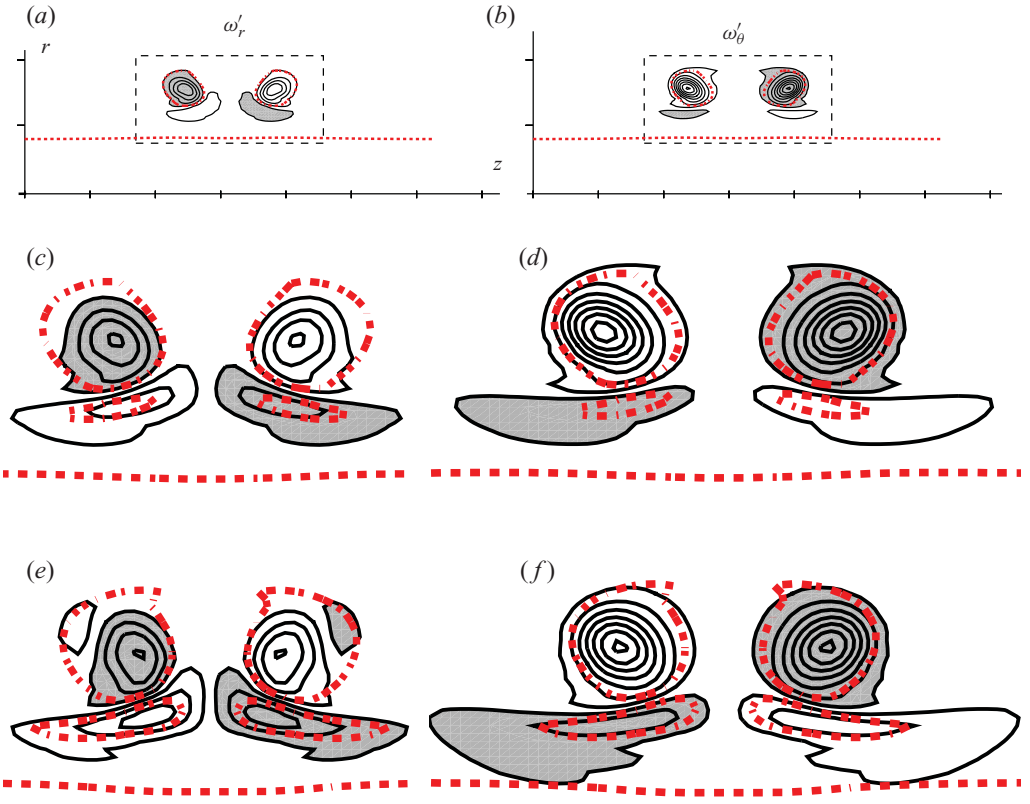


FIGURE 23. (Colour online) The ω_r' and ω_θ' contours (where grey indicates negative vorticity) for the regenerative mechanism at $Re = 10\,000$. Times shown are $t = 3$, $t = 4$ and $t = 5$ in a meridional plane rotating with the mean flow at the radius of the parent's head (i.e. the point at which the axis of the parent thread is closest to the column axis). This captures the structure of the offspring thread forming behind the head of the hairpin, as seen in figure 22. The lowest contour level for all panels is $|\omega| = 0.2$, with step size $|\delta\omega| = 0.4$. $\omega = 1$, marking the cores of the vortex column, parent thread and offspring thread, is plotted using dashed lines.

lines associated with the offspring thread, thus forming a new hairpin thread. The offspring thread has ω_θ' oriented oppositely to the parent thread (figures 23 and 21*c*). The offspring thread progressively strengthens via continued tilting of mean axial vorticity into ω_r', which then intensifies ω_θ' via the column's mean strain as shown in figure 23(*c*–*f*). Offspring vorticity intensifies even though there is significant viscous cross-annihilation, not only between the oppositely oriented parent and offspring legs, but also between the legs of the offspring thread, as the legs have oppositely oriented ω_r' and ω_θ'.

Self-induced motion in the axial direction causes the parent legs to approach each other, forming a dipole. With further evolution, the parent hairpin will migrate away from the vortex column, thereby weakening the mechanism of offspring radial vorticity generation, eventually ending offspring intensification. The legs of the offspring thread, on the other hand, migrate away from each other due to their (opposite) orientation. In this simulation, the patches of offspring vorticity do not collapse into a distinct vortex. However, it is plausible that further intensification of the offspring vorticity culminating in a fully formed offspring thread may occur and result in renewed transient growth.

https://doi.org/10.1017/jfm.2011.226 Published online by Cambridge University Press

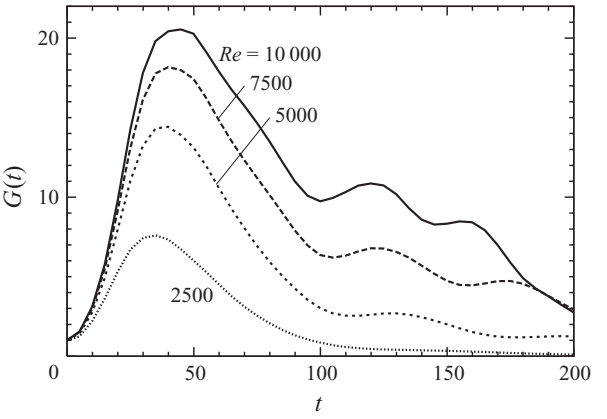


FIGURE 24. Perturbation energy evolutions for different Re, all starting with the same $Re = 5000$ optimal mode perturbation.

In the following, we discuss DNS results showing regenerative growth of a transient growth mode through a similar process.

4.7. *Simulation of regenerative growth*

We discuss here a set of simulations (different Re) initialized with the $Re = 5000$ global optimal perturbation with an initial amplitude of 4×10^{-2}; that is, the same initial perturbation mode but operating at $Re = 2500$, 5000, 7500 and 10 000. Note the difference from § 4.4, where different Re are simulated, each with its own optimal mode. Here, the perturbation is kept the same in order to capture the Reynolds number effect alone.

With increasing Re, the perturbation grows for longer durations and the peak gain also increases (figure 24) – not unexpected consequence of reduced viscous damping. The observation of interest here is that the higher-Re cases display periods of secondary energy growth in the decay phase; for example between $t = 100$ and 140. There is yet another period of growth beyond $t = 150$. No such growth is seen if the initial perturbation amplitude is reduced to levels representative of linear-regime evolution.

The parent–offspring scenario discussed earlier need not imply a cyclical process of overall energy decay followed by growth, as the mechanism of ω_r' generation through tilting of the mean vorticity may operate continually. Thereby, one may only observe perturbation energy either being sustained or decaying at a reduced rate. Cyclical energy growth, of the type seen in figure 24, on the other hand is strong indication of a regenerative mechanism at play. Each successive regenerative gain peak is lower than the previous. The trend with Re, however, does suggest that perturbation energy may be sustained at elevated levels for long periods of time at higher Re.

We present some flow visualization aimed at explaining how secondary growth occurs. As might be expected, vortex dynamics of late-time transient growth is complicated by the interactions between numerous threads and patches of perturbation vorticity. The three-dimensionality of the flow also makes it difficult to easily track individual threads as they are advected around the vortex column by the mean swirl. Nevertheless, it is possible to assert a qualitative resemblance of actual flow evolution to the cartoon in figure 21.

Figure 25 shows ω_y' and ω_x' contours (note the larger radial extent of significant ω_θ') in a meridional z–x plane, during the initial period of growth and decay for the

https://doi.org/10.1017/jfm.2011.226 Published online by Cambridge University Press

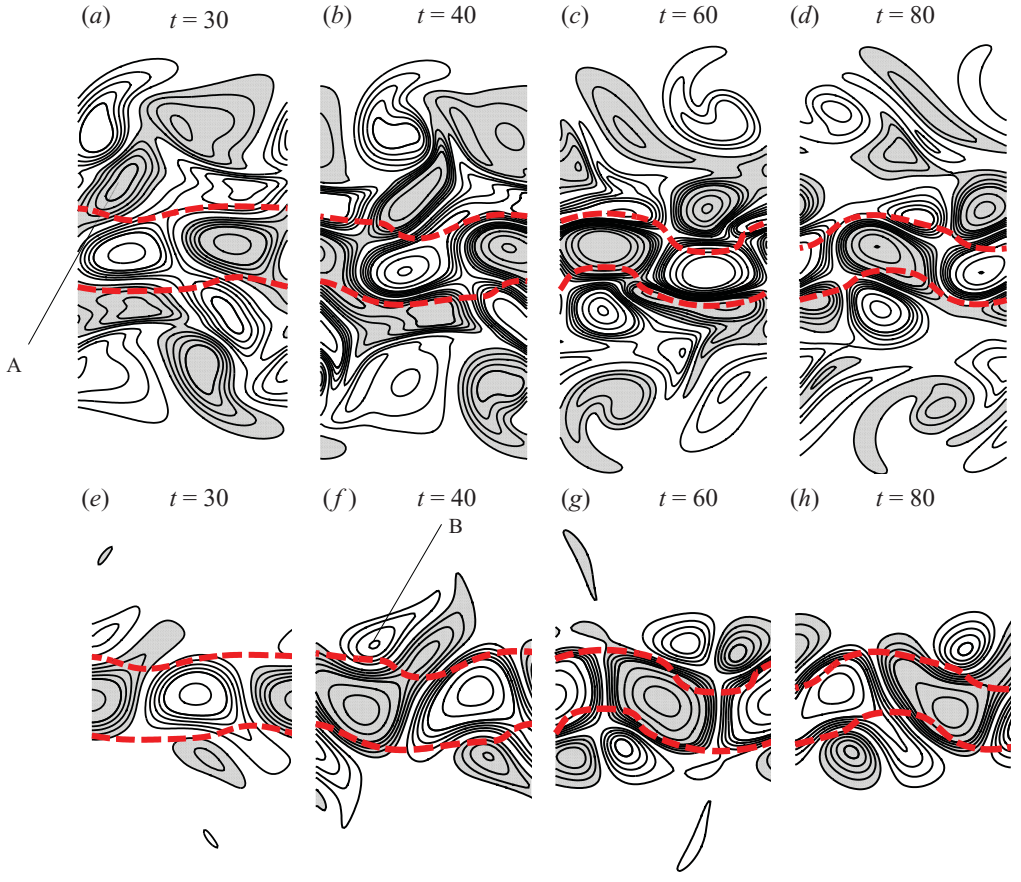


FIGURE 25. (Colour online) Perturbation vorticity contours in the meridional z–x plane during the initial period of energy growth and decay at $Re = 5000$. Plots (a–d) show ω_y' and (e–h) show ω_x'. Two ranges of contour levels are shown (to avoid crowding) in all panels; the first being $[0.04, 0.2, 0.04]$ and the second $[0.2, 0.5, 0.1]$. The thick dashed contour is $\omega = 1$ and is indicative of the vortex core.

$Re = 5000$ case, between $t = 30$ and $t = 80$. We focus on the upper half-plane (positive x), where $+\omega_y'$ coincides with $+\omega_\theta'$ and $+\omega_x'$ with $+\omega_r'$. Initial growth is associated with tilting of ω_r' present in the optimal mode (seen as weak $-\omega_r'$ in figure 25e at large radii) into the azimuthal direction and the stretching of the resulting ω_θ'. The thread labelled A in figure 25(a) intensifies through this process, as is evident from its evolution through figure 25(b–d). (Note that the thread appears to move in the $+z$ direction. This is actually opposite to the direction of self-induced motion of a thread with $-\omega_\theta'$. This motion is by the induced velocity of the stronger $+\omega_\theta'$ thread seen in figure 25(a, b) combined with its own left-handed spiral geometry, which makes it appear to move even more in the $+z$ direction as it is advected by the $+V$ mean swirl of the vortex column.) Swirl induced by the thread acts to tilt mean axial vorticity, much as in figure 21(a); hence, the adjacent patches of positive and negative ω_x' near the core, labelled B in figure 25(f). These patches of ω_x' (i.e. radial vorticity), appearing initially at $t = 30$ (figure 25e), intensify.

The net consequence of this process is that negative ω_x' (or ω_r') appears in the 'wake' of the initial thread A (i.e. trailing in z as the threads are advected around the

https://doi.org/10.1017/jfm.2011.226 Published online by Cambridge University Press

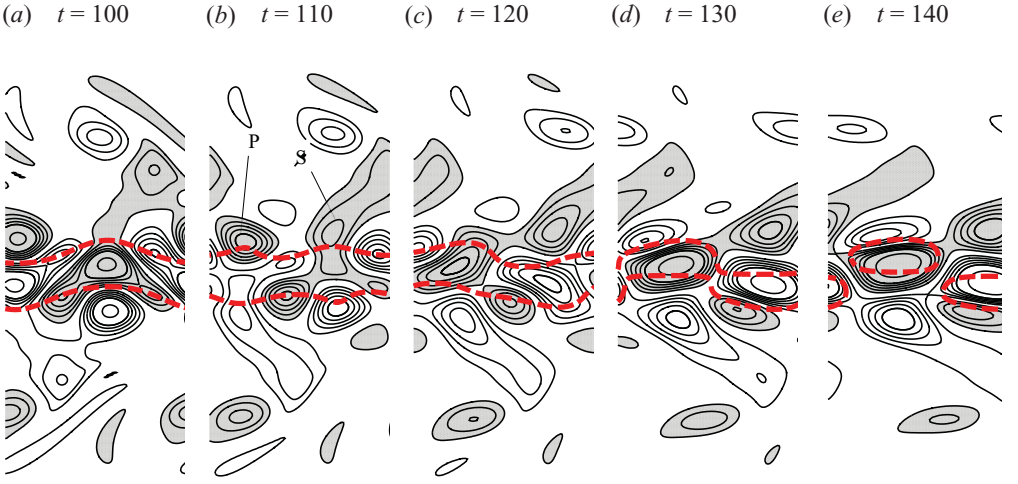


FIGURE 26. (Colour online) The ω_y' contours in the meridional z–x plane during secondary growth at $Re = 5000$, continuing the evolution shown in figure 25. The lowest contour level is $|\omega_y| = 0.02$, with increments $|\delta\omega_y| = 0.02$. Thick dashed line is $|\omega| = 1$ and denotes the vortex core.

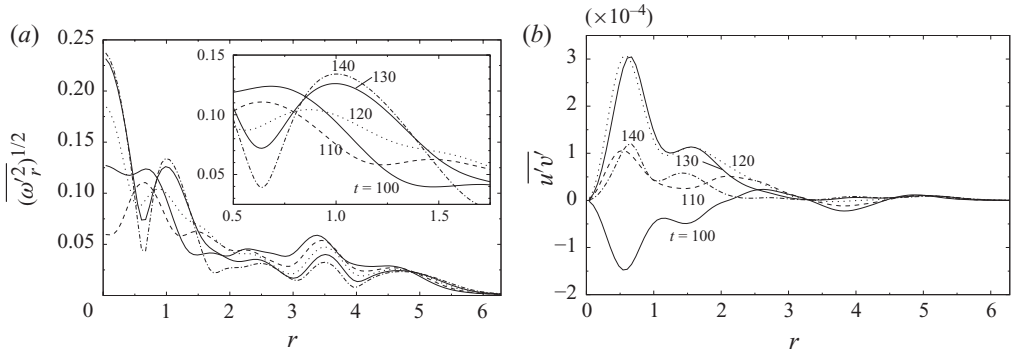


FIGURE 27. Profiles of (*a*) r.m.s. ω_θ' and (*b*) $\overline{u'v'}$ Reynolds stress, during the period of secondary growth ($t = 100$ to $t = 140$) at $Re = 5000$. In (*a*), same lines have the same t values.

column). This new ω_r' enables the vortex column's mean strain field to generate and amplify secondary ω_θ', in a manner similar to the initial growth. Note that $+\omega_r'$ would result in $-\omega_\theta'$ through this process, because the mean swirl is in the $+\theta$ direction. Figure 26 shows ω_θ' evolution during the period of secondary growth, between $t = 100$ and $t = 140$. The primary thread responsible for initial growth is labelled P, and secondary vorticity is labelled S. Azimuthal vorticity in S is along the $-\theta$ direction, as would be expected if it resulted from $+\omega_r'$ induced by P. This new azimuthal vorticity is subsequently amplified by the mean strain field near the core boundary (figure 26*b*–*d*). The proximity of new threads (formed from S) to the vortex core drives the amplification of core perturbation energy seen in figures 26(*d*) and 27(*b*).

Profiles of r.m.s. ω_θ' confirm that there is net generation of azimuthal vorticity during this period of regenerative growth (figure 27*a*). Note that at $t = 110$, r.m.s. ω_θ' has decreased substantially just outside the core. Subsequently, there is growth of r.m.s. ω_θ' due to the stretching of the secondary vorticity, in a manner similar to that

https://doi.org/10.1017/jfm.2011.226 Published online by Cambridge University Press

seen during the initial period of growth. Associated with this growth of peripheral vorticity there is also the growth of core fluctuations, which magnify fourfold from $t = 110$ to $t = 140$. As expected, amplification of r.m.s. ω'_θ also causes amplification of $+\overline{u'v'}$ Reynolds stress (figure 27*b*), and hence energy growth.

An interesting feature of the dynamics during this period of regenerative growth is the growth of an $m = 2$ mode not present in the initial condition. This can be deduced from the contours of ω'_θ in figure 26(*b*), showing that peak perturbation vorticity no longer occurs on the vortex axis. Note also that the total vorticity $\omega = 1$ contour shows a 'bulging' wave-like structure at $t = 110$. The presence of an $m = 2$ mode is confirmed by visualization (not shown) of perturbation vorticity in the cross-sectional $(x–y)$ plane. It seems that this $m = 2$ mode has a limited duration of growth, as it is no longer dominant at later times. The appearance of non-bending wave modes may be expected through the nonlinear self-interaction of the bending wave mode, and is further confirmation of the nonlinearity of the instability at this stage.

The two periods of secondary energy growth (figure 24) for $Re = 10\,000$ are associated with similar amplifications of secondary ω'_θ threads. There also, secondary growth is associated with the re-amplification of peripheral r.m.s. ω'_θ and $\overline{u'v'}$. As seen in figure 24 with increasing Re, perturbation energy levels increase at every phase of evolution. As it is presently intractable to pursue the flow to still higher Reynolds numbers, we can only speculate that this mechanism of regenerative growth would trigger the onset of sustained turbulence at Reynolds number in practical flows such as the aircraft wake.

5. Concluding remarks

DNS of transient growth into the nonlinear regime are discussed. A single bending wave mode reproduces the key qualitative features of vortex interaction with turbulence. This seems encouraging from the perspective of mechanistic modelling of the turbulent vortex, in which the essential vortex dynamics of a few dominant optimal modes is captured.

Increasing initial perturbation amplitudes decrease both the period of transient growth and the energy gain. Nevertheless, for moderate amplitude initial perturbations ($\sim$5 %), significant development of core perturbation energies and turbulence structures surrounding the vortex's core is observed. Core fluctuation intensities amplify to very high levels ($\sim$40 %), resulting in large-amplitude deformations of the column.

We have observed regenerative growth of perturbation energy at the higher end of the Reynolds numbers accessible to DNS. A parent–offspring mechanism has been postulated, in which the parent threads tilt mean axial vorticity to generate new radial vorticity perturbations near the vortex column's core. An idealized simulation of the mechanism using a hairpin thread near a column supports the hypothesized dynamics and captures the generation of offspring vorticity. While flow visualization of transient growth modes has not definitively established the parent–offspring scenario, the observed generation of ω'_r prior to secondary energy growth makes the mechanism plausible. The same ω'_θ stretching mechanism responsible for initial transient growth then generates new threads, hence cyclical energy growth. Regenerative growth strengthens with increasing Re, and it is likely that in practical flows the transient growth mechanism is able to sustain turbulence.

As energy gains increase rapidly with increasing Re it is possible that transient growth triggers core transition in practical flows, with Re four orders of magnitude

https://doi.org/10.1017/jfm.2011.226 Published online by Cambridge University Press

higher than studied herein. This phenomenon of transient growth-induced vortex transition may indeed explain the discrepancies between field observations of turbulence-enhanced vortex decay and prior numerical results.

This work was supported by the National Science Foundation grant 0554165, with computer time provided by Texas Learning and Computation Center, UH.

REFERENCES

Antkowiak, A. & Brancher, P. 2004 Transient growth for the Lamb–Oseen vortex. *Phys. Fluids* **16** (1), L1–L4.

Antkowiak, A. & Brancher, P. 2007 On vortex rings around vortices: an optimal mechanism. *J. Fluid Mech.* **578**, 295–304.

Bailey, S. C. C. & Tavoularis, S. 2008 Measurements of the velocity field of a wing-tip vortex, wandering in grid turbulence. *J. Fluid Mech.* **601**, 281–315.

Crouch, J. D. 1997 Instability and transient growth for two trailing vortex-pairs. *J. Fluid Mech.* **350**, 311–330.

Fabre, D., Jacquin, L. & Loof, A. 2002 Optimal perturbations in a four-vortex aircraft wake in counter-rotating configuration. *J. Fluid Mech.* **451**, 319–328.

Heaton, C. J. & Peake, N. 2007 Transient growth in vortices with axial flow. *J. Fluid Mech.* **587**, 271–301.

Kida, S. & Tanaka, M. 1994 Dynamics of vortical structures in homogeneous shear flow. *J. Fluid Mech.* **274**, 43–68.

Mansour, N. N. & Wray, A. A. 1994 Decay of isotropic turbulence at low Reynolds number. *Phys. Fluids* **6** (2), 808–814.

Marshall, J. S. & Beninati, M. L. 2000 Turbulence evolution in vortex dominated flows. In *Advances in Fluid Mechanics 25 (Nonlinear Instability, Chaos and Turbulence II* (ed. L. Debnath & D. N. Riahi), pp. 1–40. WIT Press.

Melander, M. V. & Hussain, F. 1993 Coupling between a coherent structure and fine-scale turbulence. *Phys. Rev.* E **48** (4), 2669–2689.

Pradeep, D. S. 2005 Mechanisms of perturbation growth and turbulence evolution in a columnar vortex. PhD thesis, University of Houston.

Pradeep, D. S. & Hussain, F. 2004 Effects of boundary condition in numerical simulations of vortex dynamics. *J. Fluid Mech.* **516**, 115–124.

Pradeep, D. S. & Hussain, F. 2006 Transient growth of perturbations in vortex column. *J. Fluid Mech.* **550**, 251–288.

Pradeep, D. S. & Hussain, F. 2010 Vortex dynamics of turbulence-coherent structure interaction. *Theor. Comput. Fluid Dyn.* **24** (1–4), 265–282.

Pringle, C. C. T. & Kerswell, R. R. 2010 Using nonlinear transient growth to construct the minimal seed for shear flow turbulence. *Phys. Rev. Lett.* **105** (15), 154502.

Rennich, S. C. & Lele, S. K. 1997 Numerical method for incompressible vortical flows with two unbounded directions. *J. Comput. Phys.* **137**, 101–129.

Schmid, P. J. & Henningson, D. S. 2001 *Stability and Transition in Shear Flows*. Springer.

Schoppa, W. & Hussain, F. 2002 Coherent structure generation in near-wall turbulence. *J. Fluid Mech.* **453**, 57–108.

Smith, C. R. & Walker, J. D. A. 1995 Turbulent wall-layer vortices. In *Fluid Vortices* (ed. S. I. Green), pp. 235–290. Kluwer.

Spalart, P. 1998 Aircraft trailing vortices. *Annu. Rev. Fluid Mech.* **30**, 107–138.

Wallin, S. & Girimaji, S. S. 2000 Evolution of an isolated turbulent trailing vortex. *AIAA J.* **38** (4), 657–665.

Zeman, O. 1995 The persistence of trailing vortices: a modeling study. *Phys. Fluids* **7** (1), 135–143.

Zhou, J., Adrian, R. J., Balachander, S. & Kendall, T. M. 1999 Mechanisms for generating coherent packets of hairpin vortices in channel flow. *J. Fluid Mech.* **387**, 353–396.

https://doi.org/10.1017/jfm.2011.226 Published online by Cambridge University Press